International Geology Review
Publication details, including instructions for authors and subscription information:
http://www.tandfonline.com/loi/tigr20

Progressive, episodic deformation in the Mexican Fold-Thrust Belt (central Mexico): evidence from isotopic dating of folds and faults

Elisa Fitz-Diaz[ac], Peter Hudleston[b], Gustavo Tolson[c] & Ben van der Pluijm[a]

[a] Department of Earth & Environmental Sciences, University of Michigan, Ann Arbor, MI, USA

[b] Department of Earth Sciences, University of Minnesota, Minneapolis, MN, USA

[c] Instituto de Geología, Universidad Nacional Autónoma de México, Ciudad Universitaria, México

Published online: 19 Mar 2014.

To cite this article: Elisa Fitz-Diaz, Peter Hudleston, Gustavo Tolson & Ben van der Pluijm (2014) Progressive, episodic deformation in the Mexican Fold-Thrust Belt (central Mexico): evidence from isotopic dating of folds and faults, International Geology Review, 56:6, 734-755, DOI: 10.1080/00206814.2014.896228

To link to this article: http://dx.doi.org/10.1080/00206814.2014.896228

International Geology Review, 2014
Vol. 56, No. 6, 734–755, http://dx.doi.org/10.1080/00206814.2014.896228

Taylor & Francis
Taylor & Francis Group

Progressive, episodic deformation in the Mexican Fold–Thrust Belt (central Mexico): evidence from isotopic dating of folds and faults

Elisa Fitz-Diaz[a,c]*, Peter Hudleston[b], Gustavo Tolson[c] and Ben van der Pluijm[a]

[a]*Department of Earth & Environmental Sciences, University of Michigan, Ann Arbor, MI, USA;* [b]*Department of Earth Sciences, University of Minnesota, Minneapolis, MN, USA;* [c]*Instituto de Geología, Universidad Nacional Autónoma de México, Ciudad Universitaria, México*

(*Received 28 November 2013; accepted 16 February 2014*)

We used illite Ar/Ar dating to obtain absolute ages of folds and shear zones formed within the Mexican Fold–Thrust Belt (MFTB). The methodology takes advantage of illite dating in folded, clay-bearing layers and the ability to obtain accurate ages from small-size fractions of illite using encapsulated Ar analysis. We applied our approach to a cross-section that involves folded Aptian–Cenomanian shale-bentonitic layers interbedded with carbonates of the Zimapán (ZB) and Tampico–Misantla (TMB) Cretaceous basins in central-eastern Mexico. Basinal carbonates were buried by syn-tectonic turbidites and inverted during the formation of the MFTB in the Late Cretaceous. Results from folds and shear zones record different pulses of deformation within this thin-skinned orogenic wedge.

Mineralogical compositions, variations in illite polytypes, illite crystallite size (CS), and Ar/Ar ages were obtained from several size fractions in limbs and hinges of the folds and in the shear zones. $1M_d$-illite polytype (with CS of 6–9 nm) dominates in two folds in the TMB while $2M_1$-illlite (with CS of 14–30 nm) dominates in the third fold, in the ZB, and in the fold/shear zone. From west (higher grade) to east (lower grade): Ar retention ages indicate shearing occurred at ~84 Ma in the westernmost shear zone, folding at ~82 Ma in the ZB with subsequent localized shearing at ~77 Ma, and Ar total gas ages constrain the time of folding at ~64 Ma on the west side of the TMB and ~44 Ma on the eastern edge. These results are consistent with the age and distribution of syn-tectonic turbidites and indicate episodic progression of deformation from west to east.

Keywords: illite; Ar/Ar dating; fold–thrust belt; progressive deformation

Introduction

Extensive work on the kinematics and evolution of fold–thrust belts of western North and South America has been done over several decades (e.g. Allmendinger *et al*. 1982; Price and Fermor 1985; Suter 1987; McClay 1992; Yonkee 1992; Philippe *et al*. 1996; McQuarrie 2004; Masini *et al*. 2010). Understanding the formation of these belts is important for several reasons, including: (1) they preserve information on tectonic interaction at convergent margins (Coney 1973; Campa-Uranga 1983; Coney and Evenchick 1994); (2) their evolution is often associated with co-genetic oil migration and the formation of ore deposits at a regional scale (McQuarrie 2004; Cooper 2007) and (3) their elevation can affect atmospheric moisture circulation and precipitation (Bookhagen *et al*. 2005; Poulsen and Jeffery 2011; Campani *et al*. 2012). The study of the Mexican Fold–Thrust Belt (MFTB) in this article utilizes results from the development of a novel method of dating deformation by using folds and shear zones exposed across strike, along an ENE–WSW cross-section of the belt. We have described the approach and the illite $^{40}Ar/^{39}Ar$ dating method of fold dating using two folds in the easternmost, lower temperature (~80–170°C) segment of the section elsewhere (Fitz-Diaz and van der Pluijm 2013). In the present study, we present complementary data from the higher temperature (180–250°C) segment on the western side of the section to elucidate the regional implications of dating for fold–thrust belt evolution.

In order to interpret the ages of these individual structures within the framework of the larger scale tectonics, we consider the critical taper model. The critical taper model theory of Davis *et al*. (1983) and subsequent refinements (Dahlen *et al*. 1984; Dahlen and Barr 1989; Dahlen 1990) link deformation within the wedge to the growth of the orogen as a whole. Wedges in fold–thrust belts are defined by a detachment surface (a basal shear zone that separates deformed wedge rocks from undeformed rocks below), often dipping to the rear of the wedge, and a topographic surface of the wedge dipping towards the toe. The model assumes that the material within the wedge is mechanically homogeneous, exhibits Mohr–Coulomb failure behaviour and everywhere is on the verge of failure. It grows by adding material at the toe or by underplating. Whereas these conditions are never

*Corresponding author. Email: elisaf@geologia.unam.mx

exactly met in nature, the evolving wedge model has been remarkably successful in accounting for first-order characteristics of natural orogenic belts (McQuarrie 2004; Stockmal *et al*. 2007; Fitz-Díaz *et al*. 2011b).

Physical and numerical models of orogenic wedges, utilizing critical taper theory, have explored different factors that affect wedge geometry/evolution, such as variations in dip of the detachment surface, differences between internal and basal friction, lateral variations of mechanical properties of rocks within the wedge, the presence of different detachment levels within the wedge, the effect of erosion and syn-tectonic sedimentation and the resulting deformation patterns and intensity of strain within the wedge vs. wedge displacement (e.g. Huiqi *et al*. 1992; Dixon 2004; Stockmal *et al*. 2007; Simpson 2009; Cruz *et al*. 2010, 2011). This modelling work has produced results generally consistent with critical taper theory and specifically has shown that: (1) deformation starts at the rear of the wedge and propagates to the front (e.g. Huiqi *et al*. 1992; Simpson 2009); (2) erosion rates are highest at the back of the wedge, associated with greater elevations (e.g. Cruz *et al*. 2010, 2011); (3) the age of syn-tectonic deposition is progressively younger towards the front of the wedge (e.g. Stockmal *et al*. 2007); and (4) exposed structures towards the rear of the wedge forms at higher temperatures than those at the front (e.g. Gray *et al*. 2001; Fitz-Díaz *et al*. 2011b; Ortega-Flores 2011).

Within the framework of this theory, we utilize Ar isotopic dating of local structures to examine the time dimension of progressive deformation within an evolving, heterogeneous fold-thrust wedge. We chose a well-exposed section in the MFTB for this study for the following reasons: (1) extensive work on deformation style/kinematics and water–rock interaction has been carried out here in recent years (Suter 1984, 1987, 1990; Carrillo-Martínez 1997; Fitz-Díaz *et al*. 2011a, 2011b, 2012), (2) mesoscopic chevron folds developed in basinal carbonate sequences (limestone interbedded with shale and chert) are pervasive along the section; and (3) deformation along the section occurred at temperatures between 80 and above 250°C (Gray *et al*. 2001; Fitz-Díaz *et al*. 2011a; Ortega-Flores 2011). The last is important because it defines the temperature window at which precipitation and transformation of illite from $1M_d$ (disordered illite lacking some characteristic reflections in XRD patterns) to $2M_1$ polytype (well-organized, muscovite-like illite in the XRD pattern) occurs in fold-thrust belts (Merriman and Frey 1999; Merriman and Peacor 1999), with illite being the mineral phase that is key to this geochronological study of fold–thrust belt evolution.

In the present work, we examine the potential for syn-tectonic illite growth in clay-rich layers sheared parallel to bedding during flexural folding of carbonate sequences (Fitz-Díaz and van der Pluijm 2013). This is similar to the way that illitization has been shown to occur along faults zones due to chemical reactions promoted by fault slip (Vrolijk and van der Pluijm 1999). We analyse illite ages in different size fractions in each of three samples (from the limbs and the hinge) of three folds, and two samples from the two limbs of an asymmetrical chevron fold (in whose forelimb a later shear zone was localized, details provided in the 'Geological framework' section) and one shear zone, which formed at different positions and temperature conditions along a cross-section of the MFTB wedge in central Mexico. This analysis provides information about the timing of illite precipitation/transformation as a function of temperature and deformation history within the wedge. At the same time, it allows us to evaluate the potential for using Ar/Ar illite ages to constrain the age of local folding and shortening within thrust sheets and as a tool for analysis of progressive deformation within evolving fold-thrust wedges.

Geological framework

Tectonic setting

Jurassic–Cretaceous subduction on the western margin of North America caused magmatism and metamorphism near the plate boundary and displacement and shortening associated with eastward-directed thrusting of the sedimentary cover rocks, on the foreland side (Armstrong 1968; Coney *et al*. 1980; Coney and Evenchick 1994; Eguiluz de Antuñano *et al*. 2000; DeCelles 2004; DeCelles *et al*. 2009, Barth *et al*. 2012). The topography related with the contraction of these rocks, since modified by subsequent tectonic processes and erosion, is regionally expressed in the Rocky Mountains Fold–Thrust Belt (RMFTB) and in the Sierra Madre Oriental or MFTB further south (Figure 1). The RMFTB was formed in the Late Cretaceous–Palaeogene (DeCelles 2004; DeCelles *et al*. 2009) and includes two important tectonic episodes and associated structures in the southwest USA, namely the Sevier and the Laramide orogenies. The Sevier belt was mostly developed in the Late Cretaceous, shows a dominantly thin-skinned deformation style and affected rocks west of the Colorado Plateau (Dickinson *et al*. 1988; Yonkee 1992; DeCelles 2004; Weil and Yonkee 2012). The Laramide or Rocky Mountain foreland province defines the eastern front of the RMFTB and shows a classic thick-skinned style. The Laramide orogeny occurred in Late Cretaceous–Palaeogene time (Allmendinger *et al*. 1982; Dickinson *et al*. 1988; Lawton and Trexler 1991). Even though the first-order observations suggest that deformation progressed from west to east in the RMFTB, the manner and timing of the alternation between Sevier and Laramide events and structures are poorly understood. This is partially due to the fact that the area where Sevier and Laramide structures

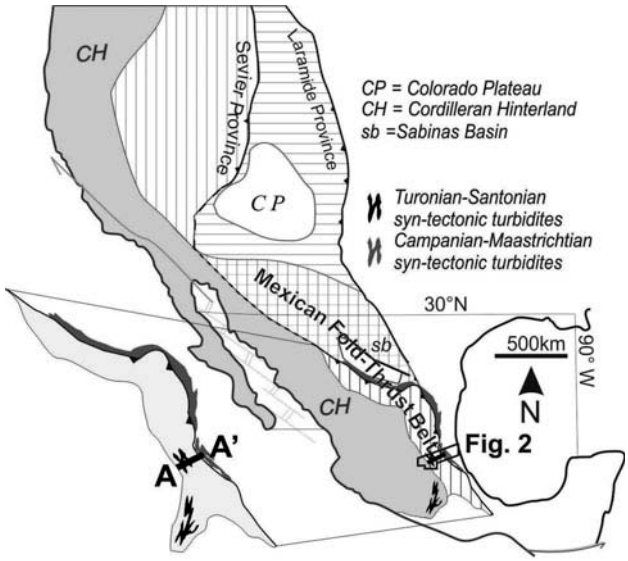

Figure 1. Tectonic map of southwestern North America showing the major tectonic features and the location of the cross-section, A–A′, where the analysed folds and shear zones occur in the Mexican Fold–Thrust Belt (MFTB). Locations where Turonian–Santonian and Campanian–Maastrichtian syn-tectonic turbidites are found on the western and eastern sides of the MFTB, respectively, are also indicated.

overlap, on the western side of the Colorado Plateau, was dismembered by the later Basin and Range extensional structures (Yonkee 1992). By contrast, in northern Mexico, the geographic separation of the Sevier and Laramide tectonic styles is lost, and high-angle reverse faults cross-cut sub-horizontal thrusts and upright tight folds (Chávez-Cabello *et al.* 2007). The kilometre-scale uplifts caused by the high-angle faults and the thick-skinned nature of these structures are obvious in large stratigraphic offsets (involving rocks of the basement) on the edges of the Sabinas Basin (Figure 1; Chávez-Cabello *et al*. 2007). Farther south, the MFTB shows a dominantly thin-skinned style, and structures are distributed along a single belt (Tardy *et al*. 1974; Eguiluz de Antuñano *et al*. 2000; Fitz-Díaz *et al*. 2011b).

A cross-section of the MFTB in central Mexico

In order to analyse the propagation of deformation within the MFTB, we targeted a narrow/condensed, continuous and well-exposed section in central Mexico (Figures 1, 2 and 4; Suter 1987; Fitz-Díaz *et al*. 2011a, 2011b, 2012). The section is oriented ENE–WSW and is about 125 km long. It covers practically the full width of the MFTB. The deformed rocks in the section define an overall wedge

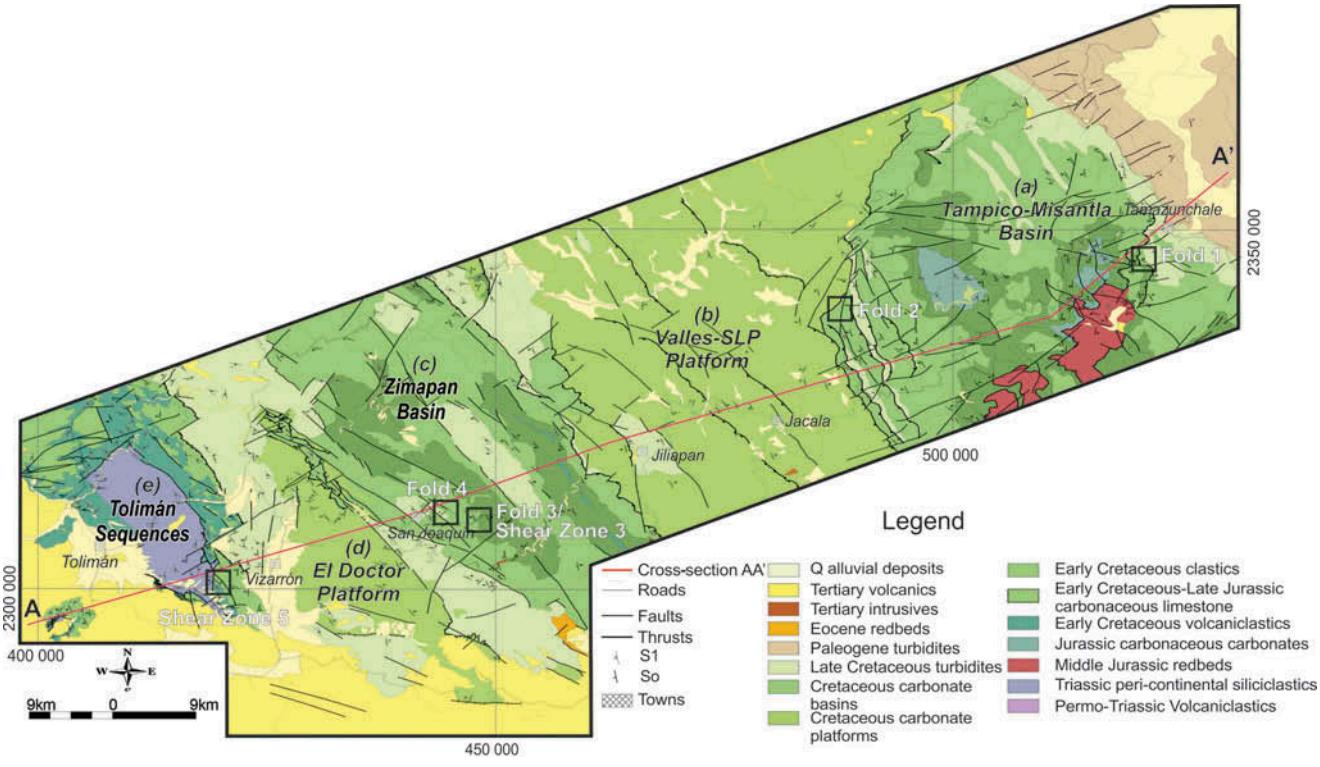

Figure 2. Simplified geologic map of the studied area in central Mexico to show the distribution of the main lithological units and palaeogeographical elements in the area, as well as the location of the cross-section in Figure 4 (modified from Fitz-Díaz *et al*. 2011b). Detailed stratigraphic columns of the different palaeogeographical elements indicated in the map are described in Figure 3.

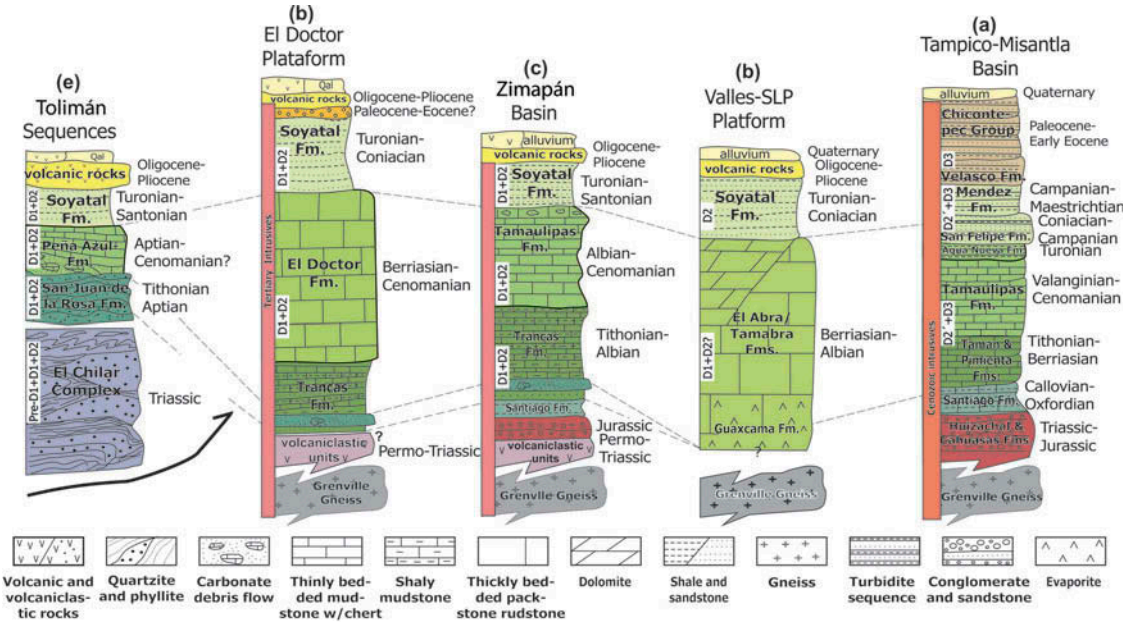

Figure 3. Chart synthesizing stratigraphic and lithological variations of units along the studied cross-section, with characteristic columns for each major palaeogeography element, see Figure 2 for location (modified from Fitz-Díaz *et al*. 2012).

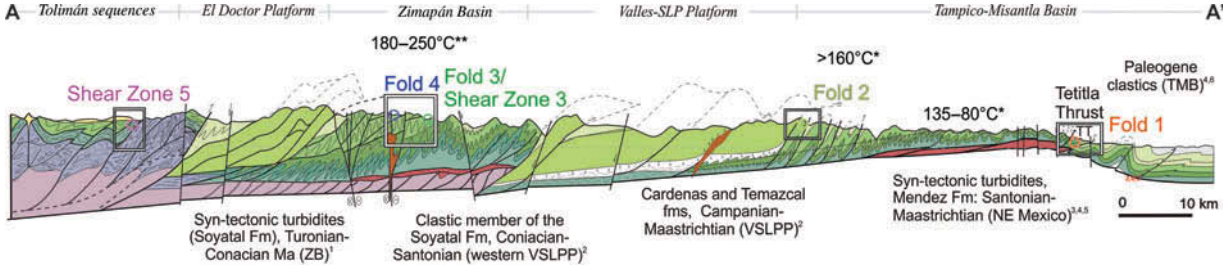

Figure 4. Regional cross-section of the Mexican fold-thrust belt in central Mexico (modified from Fitz-Díaz *et al.*, 2011a, see Figure 1 for location) showing the location of the studied folds and shear zones. Both intensity and temperature of deformation increase from east to west of the section. Local temperature of deformation was estimated with microthermometry of fluid inclusions trapped in syn-tectonic veins (Gray *et al.* 2001; Fitz-Díaz *et al*. 2011b) and vitrinite reflectance (Ortega Flores 2011). Ages of syn-tectonic turbidites are indicated (1, Hernández–Jaúregui, 1997; 2, Kiyokawa, 1981; 3, Omaña-Pulido, 2012; 4, Suter, 1990; 5, Pessagno, 1969; 6, Goldhammer, 1999; 7, López-Oliva *et al.* 1998; 8, Alzaga Ruíz *et al.* 2009).

shape tapering eastwards, with a dominantly thin-skinned deformation style (Fitz-Díaz *et al*. 2011b).

Most of the rocks involved in the deformation along the section are part of the sedimentary cover of dominantly Cretaceous carbonates (Figures 2–4; Suter 1987; Fitz-Díaz *et al*. 2011a, 2011b, 2012). A special characteristic of these carbonates is the occurrence of abrupt lateral facies changes associated with different major palaeogeographical elements across the region. These elements are, from east to west, the Tampico–Misantla Basin (TMB), the Valles–San Luis Potosí Platform (VSLPP), the Zimapán Basin (ZB) and the El Doctor Platform (EDP; see distribution in Figure 2). Stratigraphic columns characteristic of each of these palaeogeographical elements are presented in Figure 3. To the west, the carbonates are thrusted by a suite of rocks grouped as the Tolimán sequences, which consist of a siliciclastic polydeformed Triassic unit (El Chilar Complex), a Late Jurassic–Early Cretaceous volcaniclastic package (San Juan de la Rosa Formation) and an Early Cretaceous calcareous debris flow (Peña Azul Formation; Dávila-Alcocer *et al.* 2009; Fitz-Díaz *et al*. 2011b, Figures 2, 3 and 4). The Cretaceous units in the Tolimán area can be correlated with volcaniclastic and carbonate units to the east, as suggested by Ortega-Flores *et al*. (2013).

The depositional environment of the platforms and basins prior to deformation can be envisioned as interplatform troughs (e.g. the ZB between El Doctor and

VSLPPs) with shallow water banks separated by deeper water basinal deposits (Goldhammer 1999). During deformation, the carbonate sequences were incorporated into major imbricate thrust sheets and displaced eastwards. Lithological differences between the platforms and basins controlled deformation style on the large scale, the basins being dominated by intense folding and the platforms dominated by thrusting (details can be consulted in Fitz-Díaz *et al.* 2012, Figure 4). In other words, pervasive folding but relatively little displacement along thrusts is recorded in the basins, whereas significant displacement on thrusts and imbrication of thrust slices, with almost no internal deformation, is recorded in the platformal carbonates. In general, the complexity of deformation increases westwards in the section, as does temperature of deformation (from ~80 to 250°C, Fitz-Díaz *et al*. 2011a, 2011b; Fitz-Díaz *et al*. 2012), as predicted for eroded orogenic wedges tapering to the E (Dahlen and Barr 1989).

Relevant conclusions from a geometric–kinematic comparative analysis of folds formed in the carbonates in the ZB and TMB (Fitz-Díaz *et al*. 2012) are summarized as follows: (1) shortening in the basins is dominated by mesoscopic buckle chevron folds, which become progressively tighter and more flattened to the west; (2) west of the Tetitla Thrust (Figures 2 and 4), two generations of folds (F1 and F2) are observed in Cretaceous carbonates (Figure 5), with the F1 folds being close-to-tight and pervasive and the F2 folds being open and commonly localized in thinly bedded and/or fine-grained rocks; (3) F1 folds are tight to isoclinal in the ZB and open-to-tight in the TMB and have an associated cleavage; (4) F2 folds are common and developed an axial plane cleavage, S2, in fine-grained rocks in the deepest exposed rocks of the ZB, but are rare and commonly associated with metre-displacement thrusts in the TMB; (5) only one generation of open, metre- to kilometre-scale folds (F2 or F3?) is observed east of the Tetitla Thrust in the foothills, and these folds involve the regional K–T boundary angular unconformity (between a tightly folded Méndez Formation and much less internally deformed Palaeogene clastic formations, see Figure 6 in Fitz-Díaz *et al*. 2012); (6) to decide whether the folds east of the Tetitla Thrust are F2 or F3 folds is not obvious from outcrop observations, although these folds do involve Palaeogene units which are not found west of the Tetitla frontal thrust; (7) all generations of folds display a similar shortening direction, towards the WSW–ENE.

In summary, regional structural and geological analysis allows distinguishing two major deformational events in the Cretaceous carbonates along the studied section: a Late

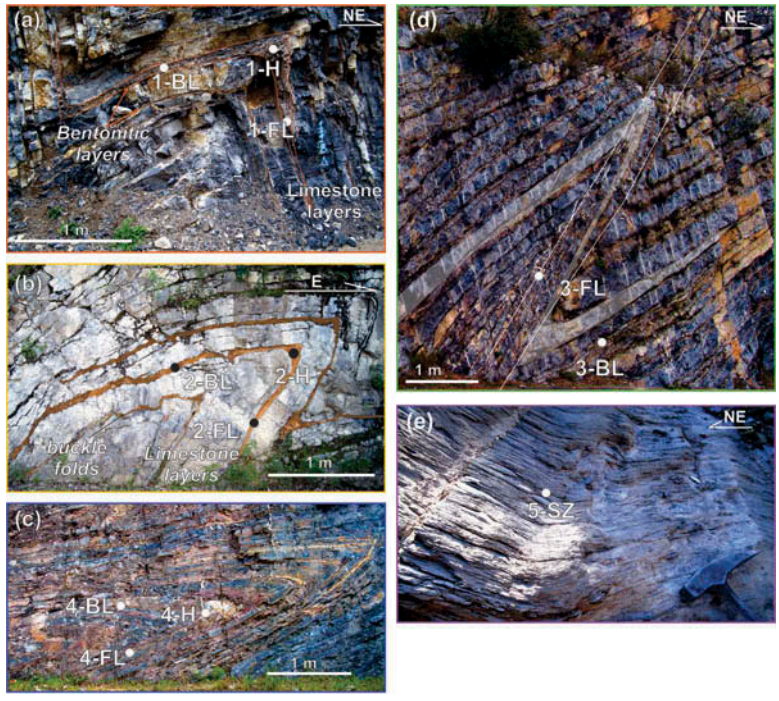

Figure 5. Photographs of outcrops from which samples of clay-rich layers were collected for mineralogical characterization and illite Ar dating, with sample locations shown by black or white dots. (a) F1 fold from the eastern edge of the TMB; (b) F1 fold from the western side of the TMB; (c) F1 fold near the centre of the ZB; (d) shear zone affecting the overturned limb of an F1 fold near the centre of the ZB; (e) strongly sheared rocks (the whole image) in the Tolimán sequence, west of the El Doctor platform, affected by later kinking. Symbols: H, hinge; FL, forelimb; BL, backlimb. See Figures 2 and 4 for location of these structures on the cross-section. Photographs in (a) and (b) are taken from Fitz-Díaz and van der Pluijm (2013).

Cretaceous D1, which affects Cretaceous rocks to the west of the Tetitla Thrust (which was presumably the frontal thrust), and a Palaeogene D2, which is responsible for folds in the foothills in the Palaeogene (Fitz-Díaz *et al.* 2012). Since the rocks west of the Tetitla Thrust are affected by a second episode of folding, it might be assumed that these folds correlate with the folds in the foothills and thus also be D2. Whether in fact the different generations of folds observed in different segments (basins) along the section were formed in two or three episodes will be addressed in this article in the light of the stratigraphic constraints and new geochronologic results. In fact, it will be shown that there are actually three deformational events rather than two: D1 is in fact two events, now D1 and D2, and what was termed D2 in Fitz-Díaz *et al.* (2012) and Fitz-Díaz and van der Pluijm (2013) now becomes D3.

In order to validate the application of the fold dating method, we compare the age of deformation with local constraints based on the biostratigraphy of Upper Cretaceous turbidites, which have been interpreted as syn-tectonic deposits on the basis of provenance studies combined with structural analyses (e.g. Hernandez-Jaúregui 1997; Gray and Lawton 2011). Several studies (e.g. Pessagno 1969; Salvador 1991; Sohl *et al*. 1991; Hernandez-Jaúregui 1997; Goldhammer 1999; Lawton *et al*. 2009; Gray and Lawton 2011) indicate that the vast majority of clastic material found in turbidites deposited in cretaceous foreland basins are derived from Cretaceous carbonates progressively uplifted from western to eastern Mexico. On the western side of the studied section, in the ZB, the age of the Soyatal Formation (syn-tectonic turbidites) is constrained to be between middle Turonian and lower Campanian (Kiyokawa 1981; Hernández-Jaúregui 1997, Figure 3). Of particular interest in this unit is a thick breccia horizon (youngest exposed layers of this unit) that contains metre-scale fragments derived from the adjacent EDP to the west, which Hernández-Jaúregui (1997) relates to local tectonic activity of El Doctor Thrust to the west of the ZB (Figures 2 and 4). High-resolution biostratigraphy (based on biozonal determination of planktonic foraminifera) in eight localities of the Soyatal Formation on the western side of the VSLPP (Omaña-Pulido 2012) constrains the age of this unit to be between Turonian and Coniacian. As in the study by Hernández-Jaúregui (1997), the stratigraphic columns produced by Omaña-Pulido show that the Soyatal Formation (Figure 3) has a lower member dominated by limestone and shale and an upper member dominated by clastic deposits (shale, sandstone and breccia). The age of the layers of the clastic upper member is Santonian according to Omaña-Pulido in the VSLPP. However, Suter (1990) reports a Campanian age for the clastic member of the Soyatal Formation on the eastern side of the VSLPP. Thus, the overall age of the Soyatal Formation on the VSLPP is considered to be Turonian–Campanian (Figures 2 and 3). Maastrichtian clastic deposits (Temascal Formation and Cárdenas Formation) deposited directly on top of Cenomanian platformal limestone were also documented by Omaña-Pulido (2012) in two localities on the VSLPP. Farther east, in the TMB (Figures 2 and 3), calcareous turbidites comparable to those of the Soyatal Formation are named the Méndez Formation, which has a Campanian–Maastrichtian age on the basis of planktonic foraminifera (Pessagno 1969; Suter 1990; López-Oliva *et al.* 1998; Goldhammer 1999, Figure 3). The Méndez Formation is critical in the interpretation of fold ages on the eastern edge of the studied section since it is affected by strong folding that produced an intense axial plane cleavage. There is an angular unconformity (K–T unconformity) that separates this unit from less deformed Palaeogene clastic deposits (Velasco Formation and Chicontepec Group, Suter 1990, Figure 3), which along with the angular K–T unconformity are folded in asymmetrical open folds with vergence to the east (Fitz-Díaz *et al*. 2012; Figure 3). These units are in turn covered by unfolded Oligocene deposits (Alzaga-Ruíz *et al.* 2009; Roure *et al*. 2009). Figures 2–4 show the relative position of folds and the age of the turbidites at different positions along the studied section.

Method

Analysed folds and shear zones

We examine three mesoscopic folds in the ZB and TMB, one shear zone modifying an F1 fold in the ZB and another shear zone in the Tolimán area (Figures 2 and 3, Table 1). These structures, all affecting Aptian–Albian carbonates, except for the shear zone in the Tolimán area, are distributed along the section and represent different stages of deformation within the MFTB. All fold hinges are sub-horizontal (Fitz-Diaz *et al*. 2012).

Fold 1 (Figure 5a) is an open, inclined chevron fold with straight limbs. It is located in the easternmost outcrops of Cretaceous rocks in the TMB. Structures associated with this fold (veins and axial planar cleavage) suggest layer shortening, leading to a chevron-fold style instability (Ramsay 1974) as the main mechanism of folding (Fitz-Díaz *et al*. 2012). It is characterized as F2–F3? based on the fact that the group of folds to which it belongs affects the K–T unconformity. Fold 2 (Figure 5b), a closed, moderately inclined chevron fold with overturned steep limb, formed in a similar way and was then flattened. It is located on the western edge of the TMB near the contact with massive limestones of the VSLPP. Since there is only one generation of folds at this location, it is not clear whether this fold is F1 or F2. To the west, Fold 4 (Figure 5c) and Fold/Shear Zone 3 (SZ-3) (Figure 5d) exemplify deformation in the ZB. Fold 4, a typical example of F1, formed as a chevron-style buckle fold that

Table 1. Description and age constraints of the five structures analysed.

Samples	Description	Interlimb angle (degrees)	Axial plane (DD/D)	Fold axis (P/T)	Age of deformation from stratigraphic constraints
Fold 1	Inclined, open, quasi-symmetrical chevron fold. Competent-layer thickness is preserved around the fold. Shale layers are considerably sheared parallel to bedding (F3)	85–80	245/60	06/335	Eocene
Fold 2	Inclined, tight, asymmetrical chevron fold. Competent layers are slightly thicker in the hinge zone compared to the limbs. Shale layers are thinner and strongly foliated in the limbs and thickened in the hinge zone (F2)	35–40	220/45	09/310	Campanian–Maastrichtian
Fold 3 (SZ-3)	Inclined, tight, asymmetrical chevron fold. Competent layers are thickened in the hinge zone compared to the limbs. The forelimb of this fold is dramatically attenuated by action of the shear zone (F1)	20–30	245/50	03/315	Turonian–Maastrichtian
Fold 4	Almost recumbent, close to isoclinal asymmetrical chevron fold. Competent layers are thickened in the hinge and considerably attenuated in the limbs, which are roughly the same in thickness (F1)	17–22	250/16	06/320	Turonian–Maastrichtian
SZ-5	Strongly foliated fine-grained tuff found at the base of the San Juan de la Rosa Formation. It is sheared in a local detachment zone that separates folded rocks in the hanging wall, from El Chilar Complex rocks	Foliation: 040/70 (DD/D)			Turonian–Maastrichtian

Note: DD/D, dip-direction/dip; P/T, plunge/trend.

was then considerably flattened and overturned, to become almost recumbent. It has a spaced (due to pressure solution) axial planar cleavage, S1 (Fitz-Díaz *et al*. 2012), with no evidence here of refolding or overprinting by a younger cleavage. In Fold/SZ-3, on the contrary, a later shear zone was localized on the forelimb of an F1 fold and is associated with veins and a secondary (S2) cleavage that cuts across an S1 cleavage related to earlier folding. It is localized in and attenuates the inverted eastern limb of the F1 fold, which is one of a train of asymmetrical folds in the studied outcrop. In this case, we focus our analysis on the superimposed shear zone, which caused the deformation history of the two limbs of the fold to differ, rather than on the fold itself. The second shear zone sample (SZ-5, Figure 5e) comes from a thicker shear zone in the Tolimán area that separates folded volcaniclastic layers of the San Juan de la Rosa Formation from more competent rocks of the El Chilar Complex, representing the local basement (Dávila-Alcocer *et al.* 2009). This shear zone is localized in a tuff horizon and is an example of the westernmost structures associated with D1. The dating of these rocks, which are volcanic in origin and do not contain detrital illite, allows for comparison with the samples from the ZB and TMB, which may contain detrital illite.

Sampling methodology

After removing the weathered surface, about 300 g of the clay-rich layers was taken from both limbs and hinges of each of the three folds (Figure 5 and Table 1). We intentionally sampled the same stratigraphic (Aptian/Albian) 100 m-thick interval (Tamaulipas Formation, Figure 3) and the same lithology for all the folds and Fold/SZ-3 in this study, in order to be able to assess the influence of regional diagenesis. Samples were taken in three locations (shown by white dots in Figure 5) in both limbs and hinges of the folds, to allow testing for variable illitization, which could be due to different deformation histories around single folds. Also, two 300 g samples were collected from SZ-3 and one from SZ-5 (Figure 2), giving 12 samples altogether.

X-ray diffraction study

X-ray diffraction (XRD) analyses in whole-rock and clay-size fractions (<2 μm for bulk, <0.05 μm for fine, 0.05–0.2 μm for fine-medium, 0.2–1 μm for medium-coarse and 1–2 μm for coarse of the equivalent sphere, using Stokes' law) were used to characterize illite and to check for the occurrence of other potassium-bearing phases. High-resolution XRD analyses in air-dried and glycolated, oriented samples permitted the determination of illite crystallinity (IC) (Kübler 1968) and the percentage of smectite in interstratified illite/smectite (Srodon 1984). The IC was calibrated following the method and standards of Warr and Rice (1994), whereas the average CS (crystallite thickness) was determined from the IC by the Scherrer equation (Moore and Reynolds 1997). The proportions of 2M1 (detrital) and $1M_d$ (authigenic) illite in the samples were determined by comparing high-resolution XRD patterns

measured in randomly oriented powder samples with model patterns by using WILDFIRE software for samples with low content of $2M_1$ illite collected in Fold 1 and Fold 2 (Reynolds 1992; Haines and van der Pluijm 2008). WILDFIRE generates synthetic XRD patterns for randomly oriented clay minerals, and these are used to iteratively model particular $2M_1$ and $1M/1M_d$ polytypes. The modelled patterns are compared in an Excel spreadsheet and best matched with experimental patterns. This allows estimating the ratio of detrital to authigenic illite for different-size fractions (Solum and van der Pluijm 2007; Haines and van der Pluijm 2008). In a similar way but using high-resolution patterns measured in standards, Owl Creek muscovite clay-size powder as a proxy for 2M1 detrital illite and the standard 1Mt1 of the Clay Mineralogical Society as a proxy for 1Md authigenic illite, were used in samples dominated with 2M1 illite (from Fold/SZ-3, Fold 4 and SZ-5), just because they better matched the patterns of these samples.

Ar/Ar illite dating

Ages were determined using an Ar/Ar illite vacuum-encapsulation method, which separately measures the fraction of recoiled ^{39}Ar during irradiation and the Ar (^{39}Ar and ^{40}Ar) retained within illite crystals as they degas during step heating in vacuum. Total gas ages (TGAs) are calculated by using both recoiled and retained argon, while retention ages (RAs) only involve retained Ar (Dong *et al*. 1995, 1997; Hall *et al*. 1997, 2000; Verdel *et al*. 2011). A number of Ar-degassing spectra from illitic material from the well-known sections of the Gulf Coast, the Welsh Basin, the New York State Basin, Cambrian pelitic rocks from the western USA, and low-temperature mineral deposits have consistently shown that (a) the amount of recoil negatively correlates with crystallite thickness, (b) TGAs represent illite precipitation ages when illite crystallites are thinner than 10 nm, and (c) RAs better suit geological constraints when crystallites are thicker than 10 nm (Dong *et al*. 1995, 1997, 2000). The amount of recoil (Ar released from the illite crystals during irradiation), age and shape of degassing patterns for different thicknesses and vacancy densities in the illite samples analysed in this paper are in good agreement with such observations. Therefore, we used TGAs for samples with illite crystallite thickness <10 nm and RAs for illite with thicknesses >10 nm.

Extensive work on illite geochronology and mineralogy in sedimentary layers (Pevear 1999) and in fault gouges (e.g. van der Pluijm *et al*. 2001; Solum and van der Pluijm 2007; Haines and van der Pluijm 2008) has shown that mixtures of $2M_1$ and $1M_d$ illite polytypes in clay-size fractions are common. Well-ordered, 2M1 illite is concentrated in coarser clay-size fractions and was typically considered detrital in origin, whereas finer, less-ordered $1M_d$ illite was grown during subsequent diagenesis and/or deformation. Based on these assumptions, ages of detrital and authigenic illite end-members can be

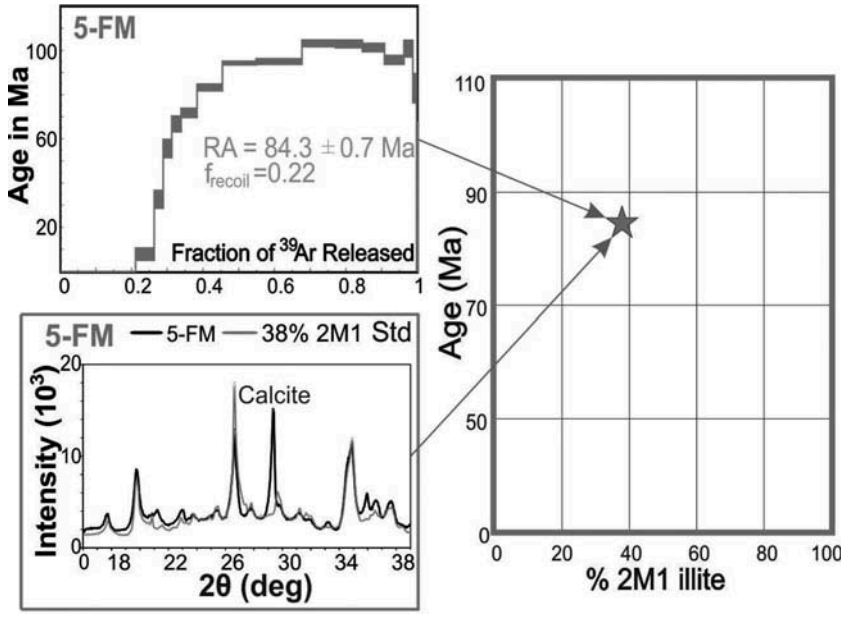

Figure 6. Illite age analysis plots of % $2M_1$ vs. age. On the upper left, Ar-degassing spectra indicating retention age (RA) used in the plot on the right. On the lower left, best fit between the experimental XRD pattern from the analysed sample and the pattern from a mixture of muscovite (38% of Owl Creek muscovite standard) and $1M_d$ illite (72%). On the right, % $2M_1$ vs. age plot of the fine-medium size fraction of sample 5.

determined using polytype quantification analysis of size fractions (Appendices 1 and 2). We plot the Ar-illite age vs. % 2M1 illite for each analysed aliquot in Figure 6 and calculate the ages at 0% 2M1 illite by using York regression, considering refinements by Mahon (1996) to determine the age of authigenic illite and corresponding standard errors of these ages (analytical-1σ and illite quantification). This procedure has been referred to as illite age analysis (IAA) (Haines and van der Pluijm 2008). The resulting ages associated with each fold and shear zone, along with local biostratigraphic ages of syn-tectonic sediments, are used to interpret the propagation of deformation within and across the MFTB.

Results

The results of the analyses are listed in Table 2. Ar-age-degassing spectra and high-resolution (0.1°/min) XRD patterns used in illite polytype quantification (with WILDFIRE model patterns) are shown in Appendices 1 and 2.

Mineralogy

There are no significant mineralogical variations from limb to hinge to limb in Fold 1, as illite/smectite, illite, kaolinite, calcite, and quartz occur in the three sampled regions in similar proportions. The minerals from Fold 2 are dominantly illite, calcite, and minor chlorite, with chlorite being less abundant in sample 2-FL, where traces of smectite, apparently interbedded with 1Md illite, were also detected in the finer fractions. For Fold/SZ-3, one sample is in the shear zone in a forelimb (3-FL) and one is outside in a backlimb (3-BL). 3-FL contains illite, kaolinite, minor chlorite, quartz, and calcite, while 3-BL contains smectite, calcite, quartz, illite/smectite, kaolinite, and chlorite. The minerals in Fold 4 are illite, illite/smectite, kaolinite, and calcite and those in SZ-5 are illite, illite/smectite, kaolinite, quartz, and albite in the coarser fractions. In general, the proportions of kaolinite, quartz, and chlorite increase as grain size coarsens, while the proportions of calcite and illite/smectite decrease. No phase containing potassium other than illite was detected in any of the analysed samples (see Figure 5 and Table 2 for sample location and results, respectively).

Localized alteration could destroy illite in shale layers and precipitate other clay minerals (e.g. discrete smectite, vermiculite) if weathering or later fractures permit interaction with surface water or hydrothermal fluids passing through these rocks. However, no sign of alteration younger than that related to folding was found in the studied outcrops.

Illite properties

IC, CS, % smectite estimates, and % 2M1 illite were determined in all clay-size fractions described above. The finest size fractions (<0.05 μm) of samples from Folds 1 and 2 and SZ-5 could not be dated because the concentration of illite was very low.

Illite is more crystalline (smaller IC) and has thicker crystallites in the coarser size fractions than in the finer size fractions, both for folds 1 and 2 (IC ~ 0.9/1.3 $\Delta 2\theta°$, CS ~ 60–90Å) and for Fold 4 and SZ-3 and SZ-5 (IC ~ 0.2–0.57 $\Delta 2\theta°$; CS ~140–300Å) compared to samples from folds 1 and 2 (IC ~ 0.9/1.3 $\Delta 2\theta°$, CS ~ 60–90Å). Analyses of XRD patterns measured in air-dried and glycolated samples show the presence of two illite polytypes, probably of discrete $2M_1$ illite and smectite interstratified with illite, which is commonly observed in the $1M_d$-rich samples. An average of 30–25% smectite was found in samples from Fold 1, 10–20% in samples from Fold 2, <10% for samples from SZ-3 and SZ-5 and practically none in samples from Fold 4 (as determined from 001/002 and 002/003 reflections in glycolated samples – cf. Table 8.3 in Moore and Reynolds 1997).

Comparison of experimental XRD patterns from randomly oriented preparations with model WILDFIRE patterns (Haines and van der Pluijm 2008) shows that the discrete illite in the samples is the well-ordered polytype (2M1) and that I/S-rich samples and/or fine-size fractions contain mostly the low-ordered polytype ($1M_d$). In samples from Fold 1, $2M_1$ illite is practically absent in the fine and fine–medium fractions, while representing approximately 7% in the medium–coarse and up to 9–10% in the coarse fractions. In the samples from Fold 2, it is about 2–5% in the finer fraction and up to 24% in the coarser fraction. It is worth noting that in samples free of 2M1, the illite polytype observed is dominantly 1M, which is Mg rich and more ordered than $1M_d$ form of illite, which is only common in hydrothermal systems. In the coarser size fraction of samples 3-FL, 4-FL, 4-H, 4-BL and SZ-5, 80–100% of the illite is $2M_1$, while in the finer fractions of these samples only 20–40% is $2M_1$. Little $1M_d$ illite was found in any size fraction of sample 3-BL. In general, CSs of illite and $2M_1$ illite increase from Fold 1 to SZ-5, while smectite content decreases. Such features indicate that the illite maturity increases westward along the cross-section of Figure 2, in agreement with predictions from thermal conditions (Fitz-Díaz *et al.* 2011a).

Ar-illite ages

Ar step-heating spectra show degassing paths, and amount of recoil (^{39}Ar released from illite crystals during neutron irradiation) varies as a function of grain size (diameter and crystallite thickness). Recoil varies between 0.44 (for average crystallite thicknesses of 6 nm and diameter of less

Table 2. Illite characterization by XRD analysis and Ar/Ar ages for the selected samples, by size fraction.

Sample	Mineralogy	IC (2θ)	CS (nm)	% smectite in I/S	Age (Ma)		Clay-size fraction	2M1 (%)
					RA	TGA		
1-FL	K, I/S, cal, and I	0.98	8	~25	60.1 ±0.9	48.7 ± 0.7	C	9 ± 2
	I/S, K, and minor cal	1.03	8	~25	67.7 ± 0.9	46.8 ± 0.7	MC	7 ± 2
	Cal, I/S, and minor qz	1.23	6	~25	67.7 ± 0.9	45.5 ± 0.4	FM	4 ± 1
1-H	K, I/S, cal, and I	0.99	8	~25	55 ± 0.5	47.9 ± 0.5	C	9 ± 2
	I/S, K, and minor cal	1.05	8	~25	61.5 ± 0.3	47.3 ± 0.2	MC	7 ± 2
	Cal, I/S, and minor qz	1.24	6	~30	61.6 ± 0.5	43.9 ± 0.4	FM	1 ± 1
1-BL	K, I/S, cal, and I	1.01	8	~30	58.9 ± 0.4	48.4 ± 0.3	C	10 ± 2
	I/S, K, and minor cal and qz	1.06	8	~30	84.2 ± 0.4	47.5 ± 0.2	MC	7 ± 2
	Cal, I/S, and minor qz	1.31	6	~30	79.1 ± 0.4	45.0 ± 0.2	FM	3 ± 1
2-FL	I, I/S, minor cal, and ch	0.90	9	~20	81.6 ± 0.2	71.8 ± 0.2	C	24 ± 3
	I, cal, and minor I/S and ch	1.09	7	~20	81.5 ± 0.3	67.4 ± 0.2	MC	15 ± 5
	I, cal, and minor I/S	1.20	7	~20	89.3 ± 0.3	62.7 ± 0.2	FM	5 ± 3
2-H	I, ch, and minor cal	0.92	9	~15	89.8 ± 0.3	76.2 ± 0.3	C	18 ± 4
	I, ch, and minor cal	1.00	8	~10	92.8 ± 0.3	75.6 ± 0.3	MC	12 ± 4
	I and minor cal and ch	0.96	8	~15	91.5 ± 0.2	71.3 ± 0.2	FM	5 ± 5
2-BL	I, ch, and minor cal	0.94	9	~15	83.5 ± 0.3	73.1 ± 0.4	C	19 ± 4
	I, ch, and minor cal	1.19	7	?	87.8 ± 0.4	73.5 ± 0.3	MC	12 ± 4
	I, and minor cal and ch	0.97	8	?	88.4 ± 0.3	68.6 ± 0.4	FM	5 ± 5
3-FL	I, I/S, K, ch, cal, and qz	0.35	23	<10	76 ± 0.4	71 ± 0.3	C	93 ± 4
	I, I/S, minor K, ch, cal, and qz	0.45	18	<10	75 ± 0.5	68.5 ± 0.4	MC	50 ± 4
	I, I/S, and cal	0.55	15	<10	77 ± 0.5	63 ± 0.4	FM	38 ± 4
	I/S and cal	0.57	14	<10	70 ± 0.5	54 ± 0.7	F	8 ± 3
3-BL	I, I/S, K, ch, and qz	0.35	23	~10	91.3 ± 1.1	71.3 ± 0.8	C	20 ± 5
	I, I/S, K, ch, and qz	0.52	16	~10	113 ± 0.8	69 ± 0.5	MC	15 ± 5
	I/S and cal	*	*	?	77 ± 0.6	50 ± 1.1	FM	10 ± 5
	I/S, cal, and ch	*	*	?	69 ± 0.7	11 ± 1	F	0
4-FL	I, K, and cal	0.36	22	<5	91.3 ± 0.5	89.6 ± 0.5	C	100 ± 1
	I, K, and cal	0.40	20	<5	84.1 ± 0.3	77.9 ± 0.4	MC	92 ± 3
	I, I/S, K, and cal	0.52	16	<5	82.9 ± 0.5	70.0 ± 0.5	FM	45 ± 3
	I, I/S, K, and cal	0.52	16	<5	84.4 ± 0.7	64.3 ± 0.6	F	35 ± 4
4-H	I, K, and cal	0.36	22	<5	84.2 ± 0.3	80.4 ± 0.3	C	98 ± 2
	I, K, and cal	0.38	21	<5	82.4 ± 0.3	77.9 ± 0.3	MC	90 ± 3
	I, I/S, K, and cal	0.52	15	<5	81.2 ± 0.3	69.8 ± 0.3	FM	50 ± 3
	I, I/S, K, and cal	0.56	14	<5	69.1 ± 0.4	51.7 ± 0.3	F	15 ± 5
4-BL	I, K, and cal	0.27	30	<5	80.1 ± 0.5	72.6 ± 0.4	C	100 ± 3
	I, K, and cal	0.21	28	<5	86.2 ± 0.4	81.5 ± 0.4	MC	95 ± 3
	I, I/S, K, and cal	0.36	22	<5	83.6 ± 0.5	68.5 ± 0.4	FM	20 ± 3
	I, I/S, K, and cal	0.36	23	<5	41.4 ± 0.4	26.3 ± 0.3	F	10 ± 5
5	I, K, qz, and ab	0.22	26	<10	85.6 ± 0.4	81 ± 0.5	C	92 ± 5
	I, K, qz, and cal	0.32	19	<10	81.3 ± 0.4	74.2 ± 0.6	MC	78 ± 4
	I, K, qz, and cal	0.37	16	<10	84.7 ± 0.6	65.7 ± 0.6	FM	38 ± 4

Notes: The main mineralogical component in the fine-medium fraction is calcite, while kaolinite is dominant in the coarse fraction. I/S, interestratified illite/smectite; I, discrete illite; ab, albite; cal, calcite; qz, quartz; ch, chlorite; K, kaolinite; IC, Illite crystallinity index (in degrees), calibrated 29. CS, crystallite size in angstrom calculated with the Scherrer equation (with $K = 0.9$ and $\lambda = 1.54$ Å25). % smectite was determined with 001/002 and 002/003 reflections in glycolated samples (Table 8.325 in Moore and Reynolds (1997)). Clay-size fractions: B, bulk, <2 μm; C, coarse, 1–2 μm-; MC, medium–coarse, 0.2 −1 μm-; FM, fine–medium, 0.05–0.2 μm. RA, Ar/Ar illite retention age; TGA; Ar/Ar illite total gas age. Ages used in IAAs are indicated with bold in the table. *Could not be measured.

than 0.05 μm) and 0.05 of the fraction of gas released (for average crystallite thicknesses of 25–30 nm and diameter between 1 and 2 μm), which are consistent with predictions from models of illite degassing by Dong *et al*. (1995, 1997) and Hall *et al*. (2000). Ar TGAs and model RAs of the 41 dated samples are listed in Table 2, and the values in bold indicate the ages used in IAA. Based on prior studies of Ar-illite dating, we use Ar TGA for samples where thicknesses of illite crystallites are <10 nm, as is the case of samples from the TMB (Fold 1 and Fold 2). Model RAs are used for illite with thicknesses >10 nm, as is the case for samples from the ZB and the Tolimán area (Fold 4, SZ-3 and SZ-5).

For samples 1-FL, 1-H and 1-BL, taken in the forelimb, hinge, and backlimb of Fold 1, respectively, Ar TGAs range from 48.7 to 45.5 Ma, from 47.9 to 43.9 Ma, and from 48.3 to 45 Ma, with analytical errors of less than or equal to 0.7 Ma. For samples 2-FL, 2-H, and 2-BL, taken in the forelimb, hinge, and backlimb of Fold 2, respectively, Ar TGAs range from 71.8 to 62.7 Ma, from 76.2 to 71.3, and from 73.5 to 68.6 M, with errors of less than 0.4 Ma. For sample 3-FL, RAs of the three coarser fraction range from 77 to 75 Ma (±0.5 Ma). The Ar-degassing spectrum for the finest clay-size fraction of this sample shows a high amount of recoil and a bimodal degassing spectrum that suggest only a small amount of illite and the additional contribution to Ar (at the highest temperatures) of another mineral phase. Similar characteristics are found in all size fractions of sample 3-BL and in the finest fractions of samples 4-BL and 4-H. Because of this, these results were no longer used in the regional analysis. RAs of all other samples from Fold 4 are consistent with a range of ages between 80 and 91 Ma, with a unimodal distribution that averages 83.5 Ma ± 2.5 Ma (1σ) with an analytical error estimate of 0.6 Ma. Finally, the RAs obtained in the three aliquots from sample SZ-5 range between 85.6 and 81.7 Ma, with analytical error estimate of 0.6 Ma (Table 2).

Discussion

The changes in clay mineralogy observed from east to west across the MFTB reflect the known progression of the metastable transformation smectite→illite→muscovite as temperature increases (Warr *et al*. 1991, 1996; Jaboyedoff and Cosca, 1999; Merriman and Peacor 1999; Merrimar and Frey 1999; Brime *et al*. 2001). In the study area, this occurs, as expected, with depth and from foreland to hinterland. The reaction illite–smectite (Fold 1), $1M_d$/1M to some $2M_1$ illite (Fold 2), and finally to dominantly $2M_1$ illite (Fold 4, Fold/SZ-3, and SZ-5) is consistent with estimates of palaeotemperature conditions at each locality (see Figure 2 and Figure 2.1 in Merriman and Peacor 1999), supporting the notion that temperature is the main factor for illite transformations (from $1M_d$ to $2M_1$) in the studied section. In the sections, we discuss how deformation plays in this scenario, in the light of Ar-illite ages and field structural observations.

Interpretation of age of deformation from IAA

The approach taken is analogous to the successful method used to date deformation in fault rocks (van der Pluijm *et al*. 2001). We plot % detrital ($2M_1$) illite vs. age for each sample (Figure 6) and use York analysis (with improvements by Mahon 1996) to determine lower and upper intercept ages (with errors) that represent authigenic and detrital illite, respectively.

The nine analysed samples (three size fractions from each of three locations) from Fold 1 fall along an age mixing line with a positive slope, with a lower intersection at 43.5 ± 0.5 Ma (Figure 7), which we interpret to be the age of authigenic illite produced during deformation. The other end of the mixing line represents the age of detrital illite. Importantly, there is no distinction between results from limbs and hinge, despite the fact that the shear is localized in the limbs. We propose that neo-illite precipitation started at the onset of shortening, thus affecting the entire clay layer, hinge zone, and limb equally, before significant fold amplification. The generation of folds to which Fold 1 belongs affects the angular unconformity at the K–T boundary as well as Palaeogene–early Eocene rocks. These folded rocks are unconformably covered by Oligocene deposits. Therefore, the calculated age of Fold 1 is consistent with the constraints of local stratigraphy in the easternmost MFTB (Figure 2; see seismic sections in Alzaga-Ruiz *et al*. 2009).

For Fold 2, which like Fold 1 displays no significant differences between limbs and hinge, we proceed in a similar manner and plot all data on a single % $2M_1$ vs. age plot. This gives us a mixing line with a lower intercept at 63.9 ± 2.2 Ma (Figure 7). Interpreted as the age of deformation, this age is consistent with the stratigraphic evidence that Late Cretaceous rocks, as young as 65 Ma (top of Méndez Formation, López-Oliva *et al.* 1998, Figure 2), are involved in the deformation in this part of the TMB. The age of Fold 2 also coincides with the emergence above the sea level of the VSLPP to the west.

In the case of Fold/SZ-3, the data are only reliable for the forelimb (3-FL) and they are distributed along an almost horizontal line on the % $2M_1$ vs. age plot (Figure 7), with an intercept at 76.9 ± 0.8 Ma for 0% $2M_1$. The absence of $2M_1$ illite and limited amount of $1M_d$ in the undeformed backlimb (3-BL) in the same layer supports the idea of illitization during the development of this shear zone. We surmise that smaller crystals of $1M_d$ illite precipitated and transformed to larger $2M_1$ illite crystals, possibly through Ostwald ripening, which is assumed to occur during a relatively narrow time window and/or with no argon loss (e.g. Merriman and

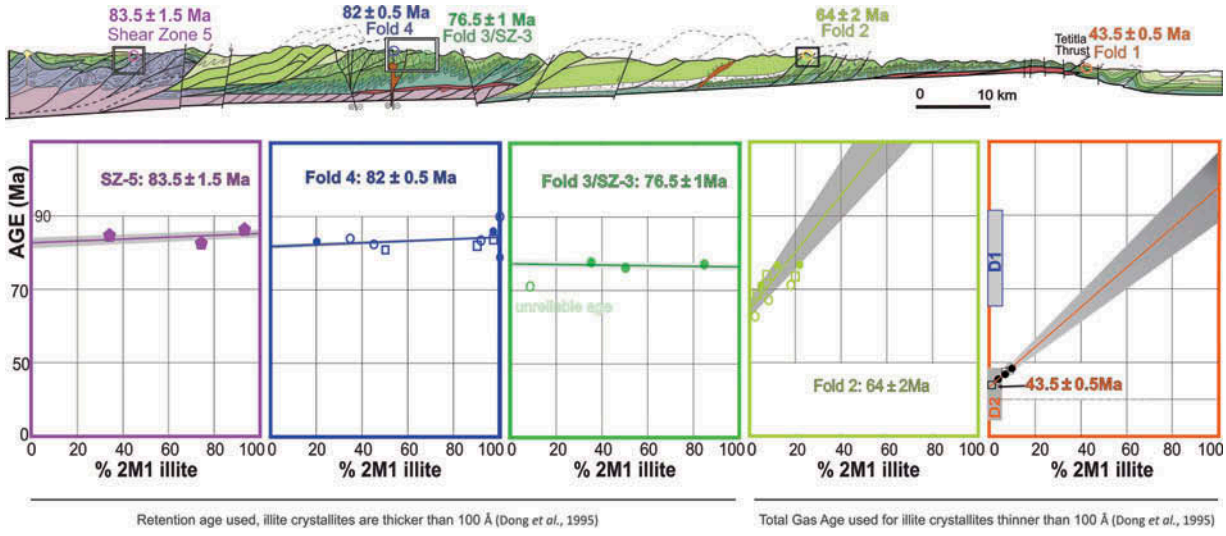

Figure 7. Plots of % $2M_1$ vs. age of size fractions of samples from three folds (1, 2 and 4) and two shear zones (Fold/SZ-3 and SZ-5). Above, the locations of the analysed folds and shear zone are indicated on the cross-section. In plots for samples from folds 1 and 2 (from the Tampico–Misantla Basin, TMB), TGAs were used because illite crystallites are thinner than 90Å (see Table 2), while RAs were used in samples from the Zimapán basin (ZB) and SZ-5 (Tolimán sequences), since illite crystallites in these samples are thicker than 14 nm (Dong *et al.* 1995). All obtained ages are younger than the deposition ages of the sampled clay-rich rocks. TGAs in the TMB and RAs in the ZB and in the Tolimán sequences make good sense with deformation constraints based on local biostratigraphy of syn-tectonic turbidites. Hollow circles correspond to samples from the backlimb, solid circles come from samples collected in the forelimb and squares come from the hinge zone, in each sampling site.

Peacor 1999; Verdel *et al.* 2011). The age of the illite in the forelimb of the fold – localized as deformation associated with SZ-3 – overlaps with a sedimentation gap and palaeokarst development (Santonian–early Campanian) on the western side of the VSLPP (Suter 1990; Omaña-Pulido 2012).

The ages for all samples from Fold 4 are distributed along an almost horizontal line that yields an age of illite growth, interpreted as the age of folding, of 82.0 ± 0.5 Ma, regardless of grain-size fraction. As for SZ-3, we conclude that progression of fine $1M_d$ illite to better-ordered $2M_1$ illite represents grain-size increase during progressive growth.

The results obtained for samples from SZ-5 are distributed along an almost horizontal line with a lower intersect at 83.5 ± 1.5 Ma (Figure 7). The ages of SZ-5 and Fold 4 are consistent with the youngest stratigraphic age of sedimentary deposition (Coniacian-Campanian) of syn-tectonic turbidites (Soyatal Formation) in the ZB and EDP (Figures 1 and 2). It is safe to assume that the tuff from SZ-5 did not contain detrital illite, and since the % $2M_1$ vs. age relationships for samples from SZ-5 are similar to those for Fold 4 and SZ-3, we conclude that detrital illite was likely absent for the latter samples also. This is in accordance with palaeogeographical reconstructions of Mexico during the Aptian–Cenomanian, which show that most of the Mexican territory was under the sea, and there were very restricted sources of sediment, mainly reworked tuffs or bentonite from western Mexico (Goldhammer 1999; Eguiluz de Antuñano *et al.* 2000). This scenario would explain the absence of detrital illite in the analysed Albian/Aptiano folded horizon.

Deformation history in an evolving orogenic wedge

The information obtained from five locations across the MFTB allows examination of the regional timing of deformation and its progression, with integration of stratigraphic and new geochronologic data. Figure 8 is a schematic model of the evolution of the MFTB in central Mexico that places the new ages in the context of an evolving, heterogeneous tectonic wedge with carbonate platforms and depositional basins (Figure 8a). Colouring on the sections shows those parts that are active within the wedge for the indicated time range (colour is coded with respect to the respective dated fold or shear zone). Syn-tectonic turbidites deposited within each time range are coloured in red. Grey and black colours are used for tectonically inactive or deactivated structures.

The western segment was the first to be activated (SZ-5 = 83.5 ± 1.5, Fold 4 = 82 ± 0.5), generating sufficient topography in the Tolimán area and EDP to provide clastic calcareous turbidites to the ZB since the middle Turonian with an increase in clastic material in the Coniacian, and onto the VSLPP in the early Santonian. The oldest syn-tectonic sediments of the Soyatal Formation suggest deformation started somewhat earlier and probably further west than the deformation recorded

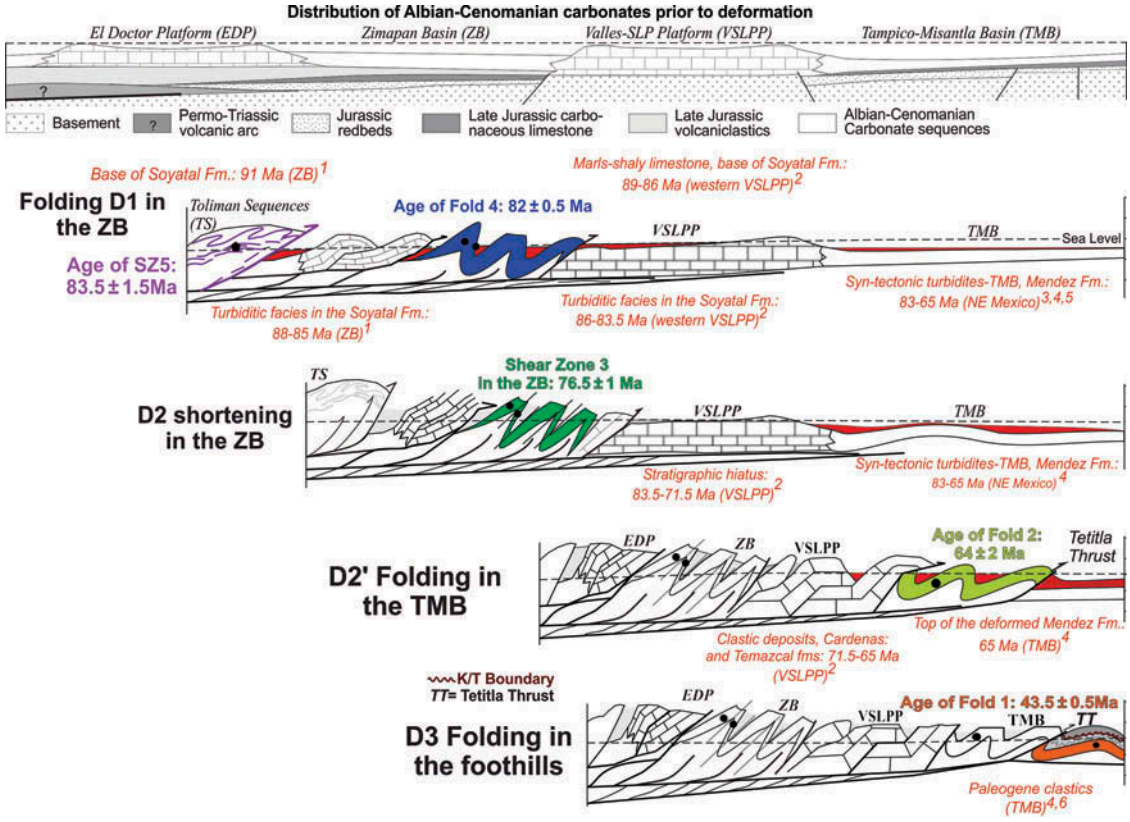

Figure 8. Schematic model of propagation of deformation of the Mexican Fold–Thrust Belt in central Mexico based on results in this article and existing geologic constraints. Deformation affected rocks of the Tolimán sequences on the western most part of the section in the Coniacian. Then, deformation propagated to the Zimapán basin causing folding (F1) until the early Campanian. In the same rocks in the middle Campanian, a second horizontal shortening pulse sub-parallel to the previous one caused attenuation of high-angle inverted forelimbs of asymmetrical folds and re-folding. On top of the VSLPP, syn-tectonic turbidites were deposited in the Coniacian–Santonian, and then upper Campanian–Maastrichtian clastic sediments were deposited directly on the platformal carbonates. The absence of a Santonian–early Campanian sedimentary record on the VSLPP implies emersion and erosion of the platform during this time, possibly caused by tectonism. Ar-illite ages suggest that folding (presumably F2) affected the westernmost TMB rocks in the upper Maastrichtian/Palaeocene, which makes good sense with the fact that these folds involve the Méndez Formation, which is as young as upper Maastrichtian. A folded unconformity separates intensely folded/foliated Campanian–Maastrichtian turbidites from less deformed Palaeogene deposits in the foothills. Folding was propagated to the foothills (coastal plain of the Gulf of Mexico) until the middle Eocene.

in SZ-5. After ~65% shortening in the ZB (Fitz-Díaz *et al.* 2012), the western part of the MFTB became a source for turbidite deposition in the TMB during the late Santonian. Figure 8b shows the wedge shape by the end of **D1** at about 82 Ma, with deformation restricted to the western part of the section. Such behaviour has been convincingly shown in analogue models involving resistant (carbonate) platform blocks with stratified sequences in adjacent basins (see MO14-IV and MO16-IV, Figure 3 in Dixon 2004).

A second episode of deformation and shortening within the belt at 77 Ma tightened early folds in the ZB and localized shear on appropriately oriented limbs of asymmetrical folds, and in addition transferred deformation to the eastern, thick VSLPP (Figure 8c). This event appears to have ended deformation in the ZB, and the western segment TA, EDP, and ZB of the section became locked. The stratigraphic gap on the VSLPP between 83.5 and 71.5 Ma (Omaña-Pulido 2012) reflects partial emergence/erosion of the platform likely due to tectonic thickening. The segment TA, EDP, and ZB plus the deforming VSLPP eventually became the backstop that transferred deformation eastward to the sedimentary rocks in the TMB. Delayed propagation of deformation may have been due to the presence of the rigid VSLPP between the basins, as observed in the analogue models by Dixon (2004).

Turbidites of Campanian–Maastrichtian ages were deposited in the TMB, and these rocks are intensely folded (Pessagno 1969; Suter 1990; López-Oliva *et al.* 1998). Fold 2 gives a minimum age estimate of 64 ± 2 Ma for deformation, which is consistent with stratigraphic correlations. Whether the shortening event that caused folding in this part of the section is related to a delayed propagation of deformation from the ZB to TMB, as suggested

above, or represents a third, separate shortening pulse, cannot be determined with the present data set. For this reason, we designate the first and most important folding event in the TMB as D2′ (Figure 8d). If Fold 2 was formed as part of a continuous D2, it took about 12 Ma for deformation to be transferred from one basin to the other.

At the eastern edge of the section, Fold 1 represents the youngest pulse of deformation affecting Cretaceous rocks at the toe of the MFTB, with an age of 43.5 ± 0.5 Ma. Because folds of this generation are open, asymmetric with vergence towards the east, restricted to the foothills, and affect the angular unconformity of the K–T boundary, involving strata as young as early Eocene (Alzaga-Ruiz *et al*. 2009), we interpret these structures as the result of a third, less intense, shortening pulse D3 in the MFTB (Figure 8e). Seismic sections from the foothills to the Gulf of Mexico show that similar folds in the foothills die out in the subsurface of the coastal plains, where they are buried under undeformed Oligocene–Pleistocene clastic deposits (Alzaga-Ruíz *et al*. 2009; Roure *et al*. 2009). Whether this deformation was induced from a subduction-related push from the west, as a continuation of wedge development, or was the result of local gravity-driven slip towards the Gulf is not clear. In any case, the local detachment surface (Santiago Formation) is locally tilted slightly to the east.

The critical taper model of thrust belt development assumes that material in the wedge is everywhere at the point of failure as the wedge grows. Thus, although the strata involved in the growing wedge get progressively younger towards the tip, other parts of the wedge should remain involved in deformation as the wedge grows. This can be seen in active accretionary fold–thrust belts such as Taiwan, where seismicity within the prism reflects ongoing deformation (Dahlen 1990; Saffer and Tobin 2011). The absence for 'out-of-sequence' deformation ages in the MFTB section suggests that either the rocks hardened with deformation and/or that the younger tectonic events were localized in widely spaced zones. The fact that deformation in the ZB and TMB is accommodated largely by chevron-style folding is supportive of the possibility that the rocks hardened, as chevron folds tend to lock as the folds tighten (Ramsay 1974). It should also be noted that in some numerical models of fold-thrust belts, segments of a developing tectonic wedge may remain relatively undeformed after first being incorporated into the wedge (see models of Stockmal *et al*. 2007).

Conclusions

The development of illite in bentonitic layers across the central MFTB is related to changing conditions of temperature across the belt, and the timing of illitization is established by Ar dating. The age of illite growth can be associated with the timing of deformation by folding or localized shear, in a manner similar to what was done previously for clays in fault zones (Haines and van der Pluijm 2008).

The analysis presented here documents the progressive development of deformation from west to east associated with the growth of the fold–thrust belt. The ages determined by Ar dating are consistent in all cases, with constraints imposed by biostratigraphic relationships. The oldest structure dated in the west, a shear zone in the Tolimán sequence, occurred at about 83.5 Ma, and the youngest deformation, a fold in the east, occurred at 43.5 Ma.

Illites from the samples collected on the eastern segment of the section are dominantly of the $1M_d$ polytype, contain smectite, and are relatively thin crystallites (≤9 nm), while illites from samples in the western segment of the section are dominantly $2M_1$ and are thicker crystallites (15–30 nm). The metastable reaction sequence smectite→$1M_d$ illite→$2M_1$ illite-muscovite from the foreland to the hinterland of the MFTB is observed in other fold–thrust belts around the world (e.g. Warr *et al*. 1991, 1996; Jaboyedoff and Cosca 1999; Merriman and Frey 1999; Merriman and Peacor 1999; Brime *et al*. 2001), reflecting progressively deeper exhumation towards the hinterland.

Integrating geochronologic data with field structural and stratigraphic relationships, we recognize three deformational events that are associated with the propagation of deformation from west to east: D1 affecting the rocks in the Tolimán area, EDP and ZB from 85–81.5 Ma; D2 localizing shear on the forelimbs of some folds in the ZB and possibly also (D2′) propagating shortening in the VSLPP and TMB, from 78 to 64 Ma and D3, which affected rocks to the east of Tetitla Thrust, in the foothills in the late Eocene at around 43 Ma (Figure 8).

Combining structural and geochronological observations allows the following general conclusions.

- The application of fold and shear zone dating across a fold–thrust belt significantly improves the resolution of timing of deformation; furthermore, applying the method in different segments allows an understanding of propagation of deformation.
- The MFTB did not evolve as a single orogenic wedge that was at failure everywhere as the wedge grew. Instead, ages show that rocks on the western side of the orogen deformed first, and after shortening and thickening, locked up and became the backstop that deformed rocks to the east.
- The MFTB represents a composite wedge that contains three belts spatially and temporally distinct, deformed during D1, D2 and D3. The distribution of these belts was influenced by the presence of two rigid platforms.
- Greater resolution of the timing of deformation will allow estimates of strain rates across the belt to be

made. In the case of the MFTB, the new data suggest relatively fast deformation on the western side of the section and in the ZB and lower deformation rates to the east.

Acknowledgements

Laboratory results were obtained at the University of Michigan; we thank Chris Hall for technical support and stimulating discussions on Ar chronology. We sincerely appreciate the reviews of Laura Webb and Sam Haines, which helped to significantly improve the quality of the original manuscript. We also thank the impressive editorial work of Professor Robert Stern.

Funding

Research was supported by a U-M Turner Postdoctoral Fellowship to EFD and National Science Foundation [grant number EAR 1118704], [grant number 1216750] to BvdP, as well as Conacyt group project [grant number 164454] to Fernando Ortega Gutiérrez.

References

Allmendinger, R.W., Brewer, J.A., Brown, L.D., Kaufman, S., Oliver, J.E., and Houston, R.S., 1982, COCORP profiling across the Rocky Mountain Front in southern Wyoming; Part 2, Precambrian basement structure and its influence on Laramide deformation: Geological Society of America Bulletin, v. 93, p. 1253–1263.

Alzaga-Ruiz, H., Lopez, M., Roure, F., and Seranne, M., 2009, Interactions between the Laramide Foreland and the passive margin of the Gulf of Mexico: Tectonics and sedimentation in the Golden Lane area, Veracruz State, Mexico: Marine and Petroleum Geology, v. 26, p. 951–973.

Armstrong, R.L., 1968, Sevier orogenic belt in Nevada and Utah: Geological Society of America Bulletin, v. 79, 429–458.

Barth, A.P., Wooden, C.E., Jacobson, J.L., and Economos, R.C., 2012, Detrital zircon as a proxy for tracking the magmatic arc system: The California arc example: Geology, v. 41, p. 223–226.

Bookhagen, B., Thiede, R.C., and Strecker, M.R., 2005, Late Quaternary intensified monsoon phases control landscape evolution in the northwest Himalaya: Geology, v. 33, p. 149–152.

Brime, C., García-Lopez, S., Bastida, F., Valin, M.L., and Sanz-López, J., 2001, Transition from diagenesis to metamorphism near the front of the Variscan regional metamorphism (Cantabrian Zone, northwestern Spain): Journal of Geology, v. 109, 363–379.

Campani, M., Mulch, A., Kempf, O., Schlunegger, F., and Mancktelow, N., 2012, Miocene paleotopography of the Central Alps: Earth and Planetary Science Letters, 337–338, p. 174–185.

Campa-Uranga, M.F., 1983, The tectonostratigraphic terranes and the thrust belt in Mexican territory, *in* Proceedings of the Circum-Pacific Terrane Conference: Stanford, CA, Stanford University Publications, Geological Sciences, v. 18, p. 44–46.

Carrillo-Martínez, M., 1997, Hoja Zimapán 14Q-E(7), resumen de la geología de la hoja Zimapan, estados de Hidalgo y Queretaro: Carta Geologica de Mexico, Serie de 1: 100,000 v. 24, p. 1–32.

Chavez-Cabello, G., Aranda-Gomez, J.J., Molina-Garza, R.S., Cossio-Torres, T., Arvizu-Gutierrez, I.R., and Gonzalez-Naranjo, G.A., 2007, The San Marcos fault: A Jurassic multireactivated basement structure in northeastern Mexico: Geology of Mexico, Celebrating the Centenary of the Geological Society of Mexico, Geological Society of America, Special Paper 422, p. 261–286.

Coney, J.P., and Evenchick, C.A., 1994, Consolidation of the American Cordilleras: Journal of South American Earth Sciences, v. 7, p. 241–262.

Coney, P.J., 1973, Plate tectonics of marginal foreland thrust-fold belts: Geology, v. 3, p. 131–134.

Coney, P.J., Jones, D.L., and Monger, J.W.H., 1980, Cordilleran suspect terranes: Nature (London), v. 288, p. 329–333.

Cooper, M., 2007, Structural style and hydrocarbon prospectivity in fold and thrust belts: a global review: Geological Society of London, special publication v. 272: p. 447–472.

Cruz, L., Malinski, J., Hernandez, M., Take, A., and Hilley, G., 2011, Erosional control of the kinematics of the Aconcagua fold-and-thrust belt from numerical simulations and physical experiments: Geology, v. 39, p. 439–442.

Cruz, L., Malinski, J., Wilson, A., Take, W.A., and Hilley, G., 2010, Erosional control of the and geometry of fold-and-thrust belts imaged in a physical and numerical sandbox: Journal of Geophysical Research B: Solid Earth, v. 115, no. 9, 15 p. art. no. B09404.

Dahlen, A., Suppe, J., and Davis, D., 1984, Mechanics of fold-and-thrust belts and accretionary wedges: Cohesive coulomb theory: Journal of Geophysical Research, v. 89, no. B12, p. 10087–10101.

Dahlen, F.A., 1990, Critical taper model of fold and thrust belts and accretionary wedges: Annual Reviews Earth Planetary Sciences, v. 18, p. 55–99.

Dahlen, F.A., and Barr, T.D., 1989, Brittle frictional mountain building 1: deformation and mechanical energy Budget: Journal of Geophysical Research, v. 94, p. 3923–3947.

Dávila-Alcocer, V.M., Centeno-García, E., Valencia, V., and Fitz-Díaz, E., 2009, Una nueva interpretación de la estratigrafía de la Región de Tolimán, Estado de Querétaro: Boletín de la Sociedad geológica Mexicana, v. 61, no. 3, p. 491–497.

Davis, D., Suppe, J., and Dahlen, F.A., 1983, Mechanics of fold-and-thrust belts and accretionary wedges: Journal of Geophysical Research, v. 88, p. 1153–1172.

DeCelles, P.G., 2004, Late Jurassic to Eocene evolution of the Cordilleran thrust belt and foreland basin system, western U. S.A: American Journal of Science, v. 304, p. 105–168.

DeCelles, P.G., Ducea, M., Kapp, P., and Zan, G., 2009, Cyclicity in Cordilleran orogenic systems: Nature Geoscience, v. 2, p. 251–257.

Dickinson, W.R., Klute, M.A., Hayes, M.J., Janecke, S.U., Lundin, E.R., McKittrick, M.A., and Olivares, M.D., 1988, Paleogeographic and paleotectonic setting of Laramide sedimentary basins in the central Rocky Mountain region: Geological Society of American Bulletin, v. 100, p. 1023–1039.

Dixon, J.M., 2004, Physical (centrifuge) modeling of fold-thrust shortening across carbonate bank margins-timing, vergence, and style of deformation, *in* McClay, K.R., ed., Thrust tectonics and hydrocarbon systems: Tulsa, OK, AAPG Memoir, v. 82, p. 223–238.

Dong, H.L., Hall, C.M., Halliday, A.N., Peacor, D.R., Merriman, R.J., and Roberts, B., 1997, $^{40}Ar/^{39}Ar$ illite dating of Late Caledonian (Acadian) metamorphism and cooling of K-bentonites and slates from the Welsh Basin, UK: Earth and Planetary Science Letters, v. 150, p. 337–351.

Dong, H.L., Hall, C.M., Peacor, D.R., and Halliday, A.N., 1995, Mechanisms of argon retention in clays revealed by laser $^{40}Ar/^{39}Ar$ dating: Science, v. 267, p. 355–359.

Dong, H.L., Hall, C.M., Peacor, D.R., Halliday, A.N., and Pevear, D.R., 2000, Thermal $^{40}Ar/^{39}Ar$ separation of diagenetic from detrital illitic clays in the Gulf Coast shales: Earth and Planetary Science Letters, v. 175, p. 309–325.

Eguiluz de Antuñano, S., Aranda-Gómez, M., and Marret, R., 2000, Tectónica de la Sierra Madre Oriental, México: Boletín de la Sociedad Geológica Mexicana, v. LIII, p. 1–26.

Fitz-Diaz, E., Hudleston, P., Siebenaller, L., Kirschner, D., Camprubi, A., Tolson, G., and Puig, T.P., 2011a, Insights into fluid flow and water-rock interaction during deformation of carbonate sequences in the Mexican fold-thrust belt: Journal of Structural Geology, v. 33, p. 1237–1253.

Fitz-Diaz, E., Hudleston, P., and Tolson, G., 2011b, Comparison of tectonic styles in the Mexican and Canadian Rocky Mountain fold-thrust belt: Geological Society Special Publication, v. 349, p. 149–167.

Fitz-Diaz, E., Tolson, G., Hudleston, P., Bolanos-Rodriguez, D., Ortega-Flores, B., and Vázquez-Serrano, A.V., 2012, The role of folding in the development of the Mexican fold-and-thrust belt: Geosphere, v. 8, p. 931–949.

Fitz-Diaz, E., and van der Pluijm, B., 2013, Fold dating: A new Ar/Ar illite dating application to constrain the age of deformation in shallow crustal rocks: Journal of Structural Geology, v. 54, p. 174–179.

Goldhammer, R.K., 1999, Mesozoic sequence stratigraphy and paleogeographic evolution of northeast Mexico: Geological Society of America, Special Paper 340

Gray, G.G., and Lawton, T.F., 2011, New constraints on timing of Hidalgoan (Laramide) deformation in the Parras and La Popa basins, NE Mexico: Boletín de la Sociedad Geológica Mexicana, v. 63, p. 333–343.

Gray, G.G., Pottorf, R.J., Yurewicz, D.A., Mahon, K.I., Pevear, D. R., and Chuchla, R.J., 2001, Thermal and chronological record of syn-to post-Laramide burial and exhumation, Sierra Madre Oriental, Mexico: AAPG Memoir, v. 75, p. 159–181.

Haines, S., and van der Pluijm, B., 2008, Clay quantification and Ar/Ar dating of synthetic and natural gouge: Application to the Miocene Sierra Mazatlán detachment fault, Sonora, Mexico: Journal of Structural Geology, v. 30, p. 525–538.

Hall, C.M., Higueras, P., Kesler, S.E., Lunar, R., Dong, H., and Halliday, A.N., 1997, Dating of alteration episodes related to mercury mineralization in the Almadén district, Spain: Earth and Planetary Science Letters, v. 148, p. 287–298.

Hall, C.M., Kesler, S.E., Simon, G., and Fortuna, J., 2000, Overlapping Cretaceous and Eocene alteration, Twin Creeks carlin-type deposit, Nevada: Economic Geology and the Bulletin of the Society of Economic Geologists, v. 95, p. 1739–1752.

Hernández-Jáuregui, R., 1997, Sedimentación Sintectónica de la Formación Soyatal (Turoniano Medio-Campaniano) y Modelado Cinemático de la Cuenca de Flexura de Maconí, Querétaro- Syntectonic sedimentation of Soyatal Formation (Middle Turonian-Campanian) and kinematic modeling the Maconi Flexural Basin [Masters Thesis]: Queretaro, Instituto Politécnico Nacional, ESIA, 120 p.

Huiqi, L., McClay, K.R., and Powell, D., 1992, Physical models of thrust wedges, *in* McClay, K.R., ed., Thrust tectonics: London, Chapman and Hall, p. 71–81.

Jaboyedoff, M., and Cosca, M.A., 1999, Dating incipient metamorphism using $^{40}Ar/^{39}Ar$ geochronology and XRD modeling: A case study from the southern Alps: Contributions to Mineralogy and Petrology, v. 135, p. 93–113.

Kiyokawa, M., 1981, Geological survey of the Pachuca-Zimapán area, central Mexico, professional report: Metal Agency of Japan and Consejo de Recursos Minerales, Estados Unidos Mexicanos, 194 p.

Kübler, B., 1968, Évaluation quantitative du métamorphisme par la cristallinité de l'illite, état des progrès realisés ces dernières années: Centre de Recherches de Pau (Societé Nationale des Petôoles d'Aquitaine), v. 2, p. 385–397.

Lawton, T.F., Bradford, I.A., Vega-Vera, J.F., Gehrels, G.E., and Jeffrey, A.M., 2009, Provenance of Upper Cretaceous-Paleogene sandstone in the foreland basin system of the Sierra Madre Oriental, Northeastern Mexico, and its bearing on the fluvial dispersal systems of the Mexican Laramide Province: Geological Society of America Bulletin, v. 121, p. 820–836.

Lawton, T.F., and Trexler, J.H., 1991, Piggyback basin in the Sevier orogenic belt, Utah, implications for development of the thrust wedge: Geology, v. 19, p. 827–830.

López-Oliva, J.G., Keller, G., and Stinnesbeck, W., 1998, El limite Cretacico/Terciario (K/T) en el noreste de Mexico, extincion de foraminiferos planctonicos. The Cretaceous-Tertiary boundary in northeastern Mexico, extinction of planktonic Foraminifera: Revista Mexicana de Ciencias Geologicas, v. 15, p. 109–113.

Mahon, K., 1996, The new "York" regression, application of an improved statistical method to geochemistry: International Geology Review, v. 38, p. 293–303.

Masini, M., Bulnes, M., and Poblet, J., 2010, Cross-section restoration: A tool to simulate deformation. Application to a fault-propagation fold from the Cantabrian fold and thrust belt, NW Iberian Peninsula: Journal of Structural Geology, v. 2, no. 32, p. 172–183.

McClay, K.R., ed., 1992, Thrust tectonics: London, Chapman and Hall, 447 p.

McQuarrie, N., 2004, Crustal scale geometry of the Zagros fold–thrust belt, Iran: Journal of Structural Geology, v. 26, no. 3, p. 519–535.

Merriman, R.J., and Frey, D., 1999, Patterns of very-Low grade metamorphism in metapelitic, *in* Frey, M., and Robinson, D., eds., Low-grade metamorphism: UK, Blackwell Science, p. 91–107.

Merriman, R.J., and Peacor, D.R., 1999, Very-low grade metapelites: mineralogy, microfabrics and measuring reaction progress, *in* Frey, M., and Robinson, D., eds., Low-grade metamorphism: Bristol, Blackwell Science, p. 10–60.

Moore, D.M., and Reynolds, R.C. Jr, 1997, X-ray diffraction and the identification and analysis of clay minerals: Oxford, Oxford University Press, 373 p.

Omaña-Pulido, M.L., 2012, Bioestratigrafia, Peleoecologia y Paleobiogeografia del Cretácico superior con base en foraminíferos de la parte occidental de la Plataforma Valles-San Luis Potosí, México [PhD Thesis]: Programa de Posgrado en Ciencias de la Tierra, Universidad Nacional Autónoma de México, 198 p.

Ortega-Flores, B., 2011, Deformación por acortamiento en la Plataforma Valles-San Luís Potosí y en la Cuenca Tampico-Misantla, porción externa del Cinturón de Pliegues y Cabalgaduras Mexicano [Masters Thesis]: Programa de Posgrado en Ciencias de la Tierra, Universidad Nacional Autónoma de México, 102 p.

Ortega-Flores, B., Solari, L., Lawton, T.F., and Ortega-Obregón, C., 2013, Detrital-zircon record of major Middle Triassic-Early cretaceous provenance shift, central Mexico: demise of Gondwana continental fluvial system and onset of back -arc volcanism and sedimentation: International Geology Review, v. 56, p. 237–261.

Pessagno, E.A. Jr, 1969, Upper Cretaceous stratigraphy of Mexico, Texas and Arkansas: The Geological Society of America Memmoir, v. 111, 130 p.

Pevear, D.R., 1999, Illite and hydrocarbon exploration: Proceedings of the National Academy of Sciences of the United States of America, v. 96, p. 3440–3446.

Philippe, Y., Colletta, B., Deville, E., and Mascle, A., 1996, The Jura fold-and-thrust belt, a kinematic model based on map-balancing: Memoires du Museum National d'Histoire Naturelle, v. 170, p. 235–261.

Poulsen, C.J., and Jeffery, M.L., 2011, Climate change imprinting on stable isotopic compositions of high-elevation meteoric water cloaks past surface elevations of major orogens: Geology, v. 39, p. 595–598.

Price, R.A., and Fermor, P.R., 1985, Structure section of the Cordilleran Foreland thrust and fold belt west of Calgary: Alberta, Geological Survey of Canada, v. 84–14, 1 sheet.

Ramsay, J.G., 1974, Development of *chevron* folds: Geological Society of America Bulletin, v. 85, p. 1741–1754.

Reynolds, R.C., 1992, X-Ray-diffraction studies of illite smectite from rocks, less-than-or-equal-to-1 Mu-M randomly oriented powders, and less-than-or-equal-to-1 Mu-M oriented powder aggregates - the absence of laboratory-induced artifacts: Clay and Clay Minerals, v. 40, p. 387–396.

Roure, F., Alzaga-Ruíz, H., Callot, J.P., Ferket, H., and Granjeon, D., 2009, Long lasting interactions between tectonic loading, unroofing, post-rift thermal subsidence and sedimentary transfers along the western margin of the Gulf of Mexico; some insights from integrated quantitative studies: Tectonophysics, v. 475, p. 169–189.

Saffer, D.M., and Tobin, H.J., 2011, Hydrogeology and mechanics of subduction zone forearcs: Fluid flow and pore pressure: Annual Reviews in Earth Planetary Sciences, v. 39, p. 157–186.

Salvador, A., 1991, The Gulf of Mexico Basin: Geological Society of America, Geology of North America Series, V. J, Geologica, 568 p.

Simpson, D.H.G., 2009, Mechanical modeling of folding versus faulting in brittle-ductile wedges: Journal of Structural Geology, v. 31, p. 369–381.

Sohl, N.F., Martínez, E., Salmerón-Ureña, P., and Soto-Jaramillo, F., 1991, Upper Cretaceous, *in* Salvador, ed., The Gulf of Mexico Basin: Geological Society of America, Geology of North America Series, v. J, p. 389–444.

Solum, J.S., and Van der Pluijm, B.A., 2007, Reconstructing the Snake River-Hoback River Canyon section of the Wyoming thrust belt through direct dating of clay-rich fault rocks: Geological Society of America, Special Paper 433, p. 183–196.

Srodon, J., 1984, X-ray powder diffraction identification of illitic materials: Clays and Clay Minerals, v. 32, p. 337–349.

Stockmal, G.S., Beaumont, C., Nguyen, M., and Lee, B., 2007, Mechanics of thin-skinned fold and thrust belts, insights from numerical models: Geological Society of America, Special Paper 433, p. 63–98.

Suter, M., 1984, Cordilleran deformation along the eastern edge of the Valles- San Luís Potosí carbonate platform, Sierra Madre Oriental thrust and fold belt, east-central Mexico: Geological Society of America Bulletin, v. 95, p. 1387–1397.

Suter, M., 1987, Structural traverse across the Sierra Madre Oriental fold-thrust belt in east-central Mexico: Geological Society of America Bulletin, v. 98, p. 249–264.

Suter, M., 1990, Hoja Tamazunchale 14Q-(5), con geología de la hoja Tamazunchale, estados de Hidalgo, Querétaro y San Luís Potosí: UNAM, Instituto de Geología, Carta Geológica de México, serie 1:100,000, 56 p.

Tardy, M., Longoria, J.F., Martínez-Reyes, J., Mitre, L.M., Patiño, S.M., Podilla, R., and Ramírez, C., 1974, Observaciones generals sobre la estructura de la Sierra Madre Oriental: La aloctonia del conjunto cadena alta Altiplano Central entre Torreon, Coahuila y San Luis Potosi, Mexico: Revista del Instituto de Geología, UNAM, v. 75, p. 1–11.

van der Pluijm, B.A., Hall, C.M., Vrolijk, P.J., Pevear, D.R., and Covey, M.C., 2001, The dating of shallow faults in the Earth's crust: Nature (London), v. 412, no. 6843, p. 172–175.

Verdel, C., Niemi, N., and van der Pluijm, B., 2011, Variations in the illite to muscovite transition related to metamorphic conditions and detrital muscovite content: Insight from the paleozoic passive margin of the Southwestern United States: Journal of Geology, v. 119, p. 419–437.

Vrolijk, P., and van der Pluijm, B.A., 1999, Clay gouge; questions in structural geology; 20th anniversary special issue: Journal of Structural Geology, v. 21, p. 1039–1048.

Warr, L.N., Greiling, R.O., and Zachrisson, E., 1996, Thrust related very low grade metamorphism in a marginal part of an orogenic wedge, Sacandinavian Celedonines: Tectonics, v. 15, p. 1213–1229.

Warr, L.N., Primmer, T.J., and Robinson, D., 1991, Variscan very low-grade metamorphism in southwestern England: a diastathermal and thrust-related origin: Journal of Metamorphic Geology, v. 9, p. 1213–1229.

Warr, L.N., and Rice, A.H.N., 1994, Interlaboratory Standardization and Calibration of Clay Mineral Crystallinity and Crystallite Size Data: Journal of Metamorphic Geology, v. 12, p. 141–152.

Weil, A.B., and Yonkee, W.A., 2012, Layer-parallel shortening across the Sevier fold-thrust belt and Laramide foreland of Wyoming: spatial and temporal evolution of a complex geodynamic system: Earth and Planetary Science Letters, v. 357–358, p. 405–420.

Yonkee, W.A., 1992, Basement-cover relations, Sevier orogenic belt, northern Utah: Geological Society of America Bulletin, v. 104, p. 280–302.

Appendix 1

$^{40}Ar/^{39}Ar$-degassing spectra obtained in the (three and four) different clay-size fractions from the 11 analysed samples collected in four folds and one shear zone.

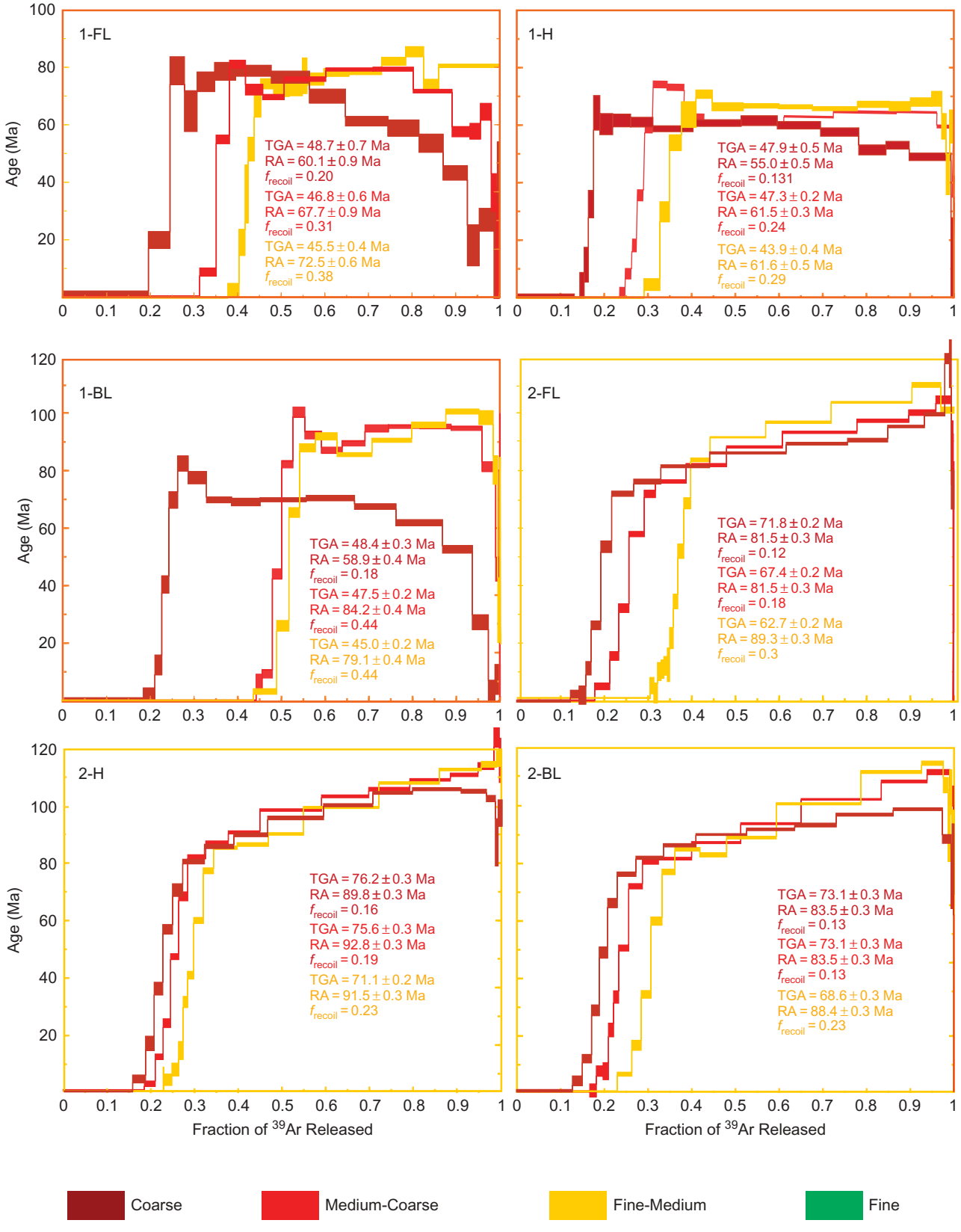

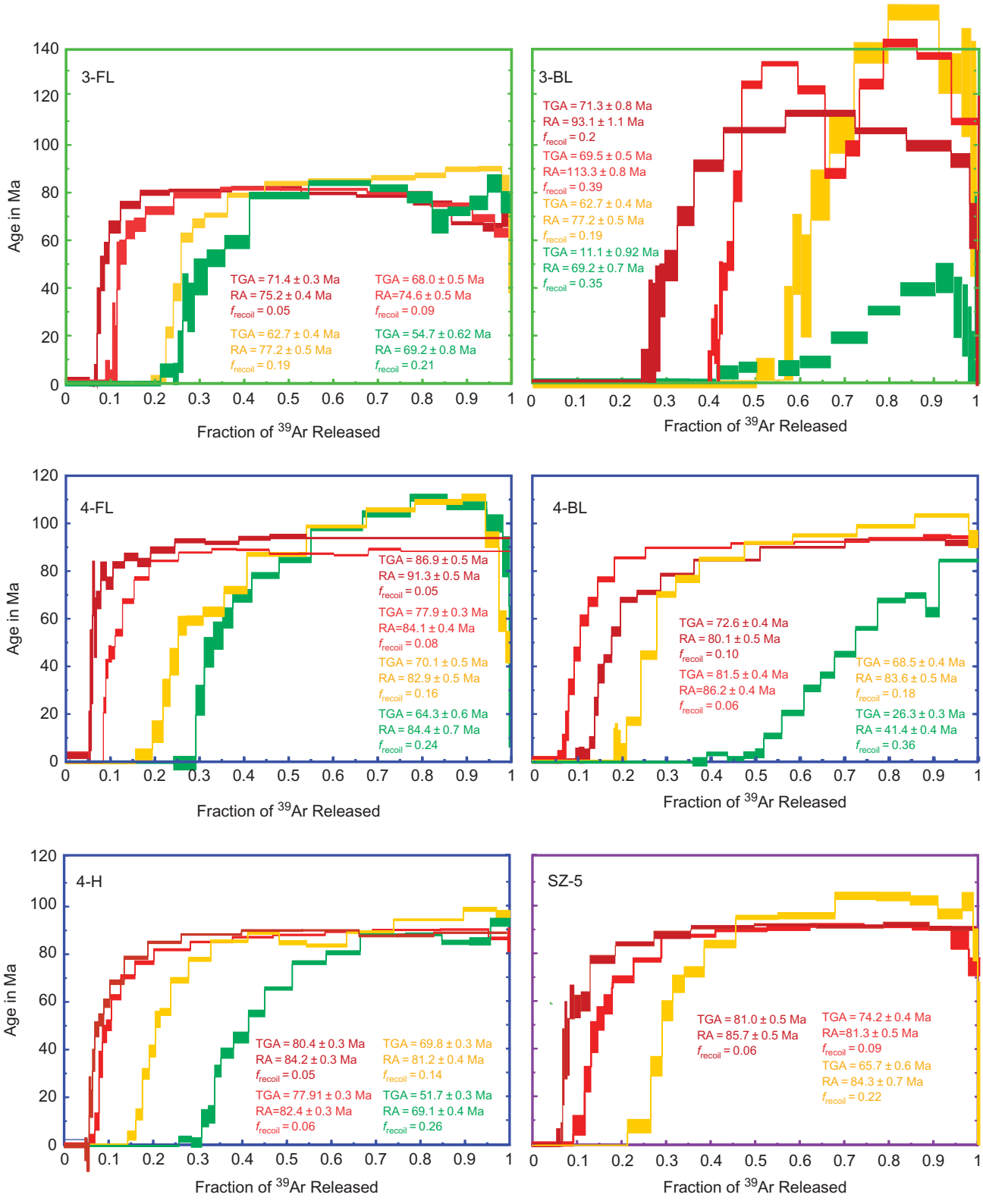

Appendix 2

Illite polytype characterization. Plots of experimental XRD patterns vs. WILDFIRE model patterns of different mixtures of 2M1 and 1Md illite for each size fraction of the analysed samples.